Supporting Information

Hydrogen evolution boosted by moderate Co$_3$ZnC with current densities beyond 1000 mA cm^{-2}

Xiaobo He, [a] Yanling Zhao, [a] Yuanchu Dong, [a] Fengxiang Yin [a]*, Xin Lin, [b] Ruilong Ma [a] and Jiaqi Li [a]

[a] Jiangsu Key Laboratory of Advanced Catalytic Materials and Technology, School of Petrochemical Engineering, Changzhou University, Changzhou 213164, China

[b] College of Chemical Engineering, Beijing University of Chemical Technology, Beijing 100029, PR China

*Corresponding author

Tel.: +86-519-86330253

E-mail: yinfx@cczu.edu.cn (F. Yin)

Contributions of authors

Xiaobo He: Conceptualization, Methodology, Writing – original draft and Writing – review & editing; Yanling Zhao: Data curation, Formal Analysis and Investigation; Yuanchu Dong: Formal Analysis and Investigation; Fengxiang Yin: Funding acquisition and Project administration; Xin Lin: Formal Analysis and Investigation; Ruilong Ma: Investigation; Jiaqi Li: Investigation.

1. Experimental

1.1 Syntheses of bimetal ZIF(ZnCo) and the resultant catalysts

In a typical synthesis of bimetal ZIF(ZnCo) with a fed molar ratio of Zn:Co of 3:7, 0.0135 mol of $Zn(NO_3)_2 \cdot 6H_2O$ and 0.0315 mol $Co(NO_3)_2 \cdot 6H_2O$ were dissolved into anhydrous methanol (250 mL) as Solution A. Meanwhile, Solution B containing 0.18 mol of 2-methylimidazole was also prepared by another 250 mL of anhydrous methanol. Then, the Solution A was dropwise added into the Solution B with slowly stirring. After stirring for another 24 h at room temperature, the purple precipitates were collected by centrifugation and washed with anhydrous methanol. The bimetal ZIF(ZnCo), i.e., ZIF(ZnCo-3:7), was finally obtained after dried at 80 °C overnight under vacuum. During the similar synthetic procedures, the control bimetal ZIF(ZnCo) with different fed molar ratios of Zn:Co, including 1:9, 5:5 and 7:3, were also synthesized, keeping the total molar quantity of Zn and Co constant (i.e., 0.045 mol). They were referred to ZIF(ZnCo-1:9), ZIF(ZnCo-5:5) and ZIF(ZnCo-7:3), respectively. In addition, ZIF-67 with only Co and ZIF-8 with only Zn were also prepared, using 0.045 mol of $Co(NO_3)_2 \cdot 6H_2O$ and 0.045 mol of $Zn(NO_3)_2 \cdot 6H_2O$, respectively.

To obtain the resultant catalysts, the pyrolysis of those ZIF(ZnCo) or ZIF-67 or ZIF-8 was carried out in N_2 at 650 ºC with the ramping rate of 5 ºC min^{-1}. The products were washed with anhydrous methanol and dried at 80 °C under vacuum overnight. The resultant catalysts were denoted as ZIF(ZnCo-1:9)-650N_2, ZIF(ZnCo-3:7)-650N_2, ZIF(ZnCo-5:5)-650N_2 and ZIF(ZnCo-7:3)-650N_2, ZIF-67-650N_2 and ZIF-8-650N_2, respectively. In addition, the samples from ZIF(ZnCo-3:7), which were

prepared at different pyrolysis temperatures (500, 700 and 800 $^{\circ}$C), were labeled as ZIF(ZnCo-3:7)-500N$_2$, ZIF(ZnCo-3:7)-700N$_2$ and ZIF(ZnCo-3:7)-800N$_2$, respectively.

1.2 Characterizations

The crystal structure of the resultant catalysts was analyzed by using X-ray powder diffraction (XRD, Smartlab 9, Rigaku, Japan) with Cu $K\alpha$ radiation (Cu K_{α}, λ = 1.5406 Å). The morphology was observed by scanning electron microscopy (SEM, SUPRA55, Zeiss, Germany). Transmission electron microscopy (TEM) and high-resolution TEM (HRTEM) images were collected on Tecnai G^2 F20 S-TWIN (FEI, U.S.A.). The energy dispersive spectroscopy (EDS) mapping was acquired on an EDS spectrometer (AztecX-Max80, Oxford Instruments, U. K.) that was attached to Tecnai G^2 F20 S-TWIN. The surface compositions, chemical states and valence band spectra were investigated by X-ray photoelectron spectroscopy (XPS, ESCALAB 250Xi, Thermo Fisher Scientific, U.S.A.). All the binding energies were calibrated to the C 1s peak at 284.6 eV. ICP-MS (Agilent ICP-MS 7900, U.S.A.) was performed to determine the possible presence of trace Pt in the resultant catalysts. N$_2$-sorption isotherms were measured at 77 K by an analyzer (3Flex, Micromeritics, USA). Specific surface areas were determined via Brunauer-Emmett-Teller (BET) method.

Electrochemical measurements

Prior to various electrochemical measurements, the ink for working electrode was first prepared. Typically, 2 mg of the resultant catalysts (or 20 wt% Pt/C) and 60 μL of Nafion solution (5 wt%, DuPont) were added to 1 mL of ethanol. After ultra-sonication for 30 min, a homogeneous ink was achieved. ~33 μL of the ink was then

casted on a glassy carbon electrode (GCE, 0.126 cm^{-2}). The catalyst mass loading of geometry is ~0.5 mg cm$^{-2}_{disk}$. For comparison, 20 wt% Pt/C was used as a benchmarked HER catalyst with the mass loading of ~0.5 mg cm$^{-2}_{disk}$ (~100 μg_{Pt} cm$^{-2}_{disk}$).

The electrochemical measurements were performed using a rotating disk electrode (RDE) apparatus and an electrochemical workstation (CHI 760E) with a typical three-electrode configuration at room temperature. A KCl-saturated Ag/AgCl electrode and a carbon rod were used as the reference and counter electrodes, respectively. All the final potentials were calibrated to a reversible hydrogen electrode (RHE) scale using the Nernst equation $E_{RHE} = E_{Ag/AgCl} + 1.022$ V (in 1 M KOH) and corrected for iR loss. The HER linear sweep voltammetry (LSV) curves were recorded from 0.1 to -0.4 V at a sweep rate of 5 mV s^{-1} and at 1600 rpm in N$_2$-saturated 1 M KOH at room temperature. In addition, the poisoning tests were carried out under the similar measurement conditions except the N$_2$-saturated 1 M KOH with 50 mM KSCN as poisoning agent.

To assess HER durability, the cyclic voltammetry (CV) cycling was performed for 20000 cycles at 50 mV s^{-1} within the potential range from 0.1 to -0.4 V. Before and after the CV cycling, the LSV curves were recorded at 5 mV s^{-1} and at 1600 rpm. In addition to CV cycling, chronopotentiometry (η-t, where η represents potential and overpotential, respectively) was also applied to evaluate the HER durability. It was performed at a constant current density of 500 mA cm^{-2} for 108 h.

The electrochemical impedance spectroscopy (EIS) measurements were carried

out at open circuit potential with a frequency range from 10^6 Hz to 1 Hz.

The electrochemically active surface areas (ECSAs) are determined by the CV curves within the potential ranges of 100 mV without Faradaic responses centered at open circuit potential and at different scan rates (10, 20, 30, 40 and 50 mV s^{-1}). The variations between anode and cathode currents at open circuit potential (i.e., $\Delta j = j_a -j_c$) are plotted with the scan rates. The half of the slopes of these plots are the electric double layer capacitance (C_{dl}), which is proportional to the ECSAs.

2. Supporting Figures
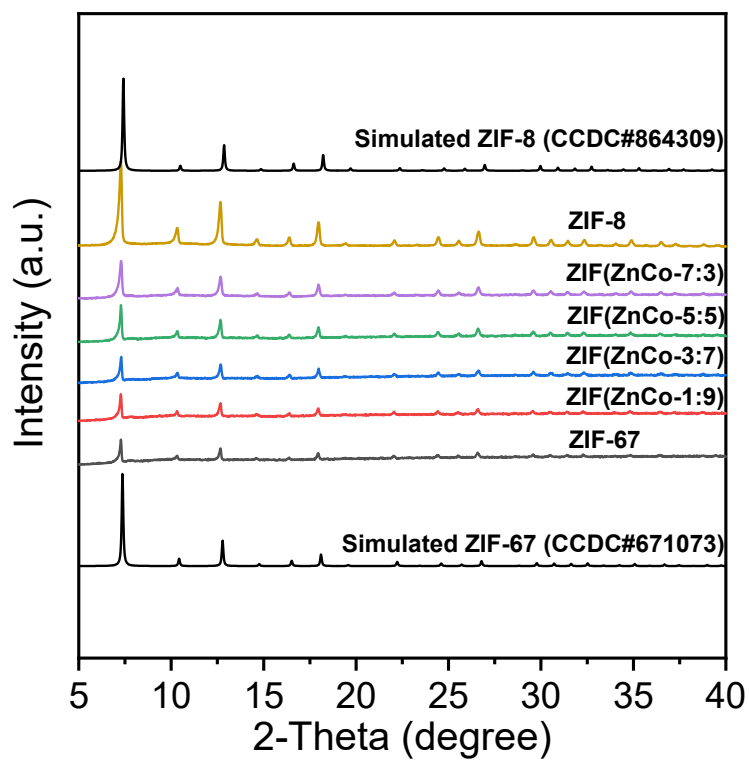
Fig. S1 XRD patterns of the prepared bimetal ZIF(ZnCo), ZIF-67 and ZIF-8. The simulated ones of ZIF-67 and ZIF-8 are based on the deposited structures with CCDC#671073 and #864309, respectively.
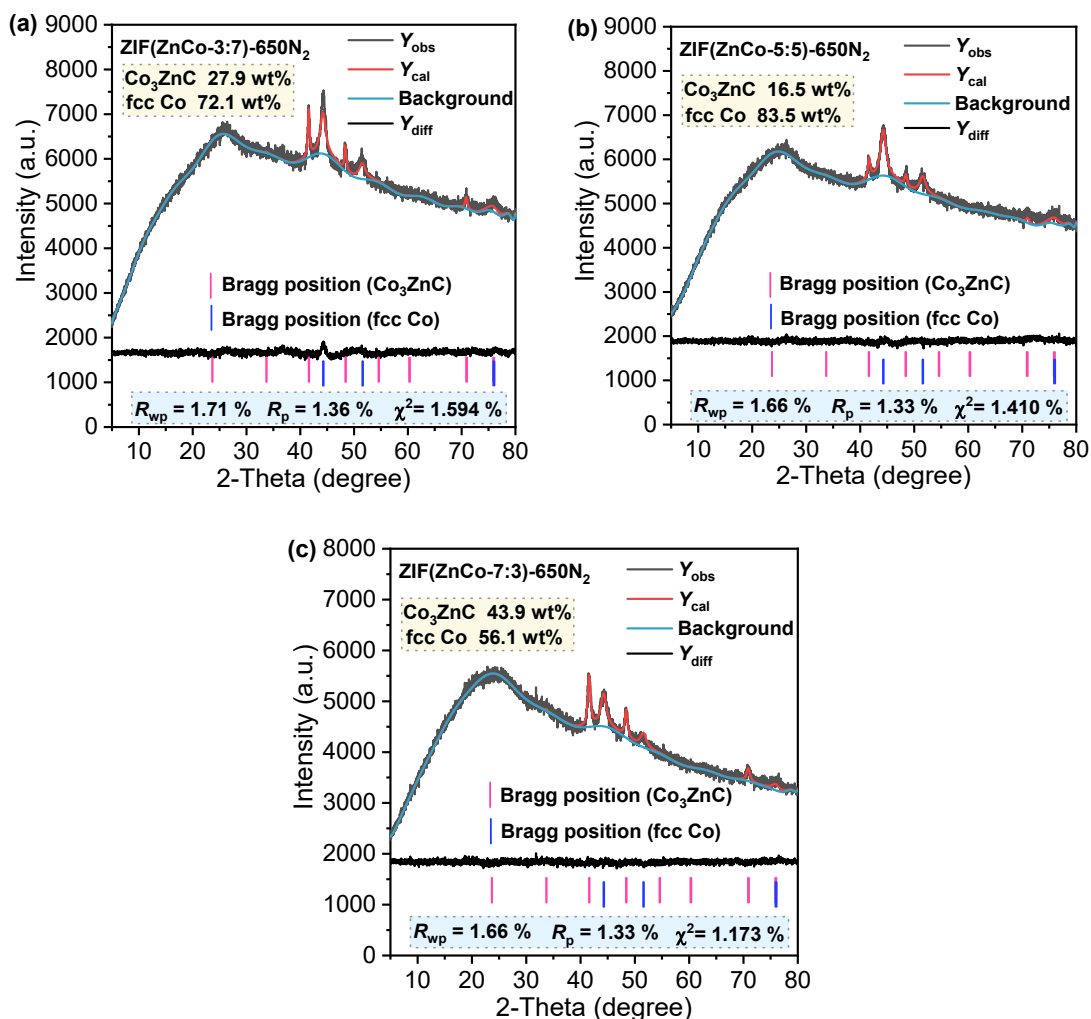
Fig. S2 The Rietveld refinement of the typical XRD patterns with backgrounds for (a) ZIF(ZnCo-3:7)-650N$_2$, (b) ZIF(ZnCo-5:5)-650N$_2$ and (c) ZIF(ZnCo-7:3)-650N$_2$.

Note S1 The Rietveld refinements of the XRD patterns of ZIF(ZnCo-3:7)-650N$_2$, ZIF(ZnCo-5:5)-650N$_2$ and ZIF(ZnCo-7:3)-650N$_2$ were conducted by using GSAS software [*J. Appl. Cryst.*, 2001, **34**, 210-213.]. The used ICSD (The Inorganic Crystal Structure Database) numbers for Co$_3$ZnC and fcc Co are #76797 and #622443, respectively. As shown in Fig. S2, the refinement parameters including R_{wp}, R_p and χ^2 are all very small, which indicates the good reliability of the refinement results. Of noted, in order to better determine the weight ratios of Co$_3$ZnC:fcc Co, the broad

diffraction peaks (2θ = ~26.5 °) attributed to the (002) planes of carbons were treated as the backgrounds during the refinements. As a result, the weight ratios of Co_3ZnC:fcc Co in ZIF(ZnCo-3:7)-650N_2, ZIF(ZnCo-5:5)-650N_2 and ZIF(ZnCo-7:3)-650N_2 are ~0.387, ~0.198 and ~0.783. Furthermore, the other three independent syntheses for ZIF(ZnCo-3:7)-650N_2, ZIF(ZnCo-5:5)-650N_2 and ZIF(ZnCo-7:3)-650N_2 (from the preparations of bimetal ZIF(ZnCo) to the pyrolysis of them) were also carried out and the XRD Rietveld refinements got the similar results to those above. Specifically, for ZIF(ZnCo-3:7)-650N_2, 27.4, 26.9 and 28.1 wt% of Co_3ZnC were obtained for the other three syntheses; for ZIF(ZnCo-5:5)-650N_2, 16.8, 15.8 and 16.1 wt% of Co_3ZnC were achieved; and for ZIF(ZnCo-7:3)-650N_2, 44.3, 43.7 and 44.5 wt% of Co_3ZnC were got. The corresponding weight ratios of Co_3ZnC:fcc Co are ~0.377, ~0.368 and ~0.391 for ZIF(ZnCo-3:7)-650N_2; ~0.202, ~0.188 and ~0.192 for ZIF(ZnCo-5:5)-650N_2; and ~0.795, ~0.776 and ~0.802 for ZIF(ZnCo-7:3)-650N_2. Thus, the mean weight ratios of Co_3ZnC:fcc Co for the four syntheses are ~0.381±0.010 (~2.62% of relative standard deviation, RSD) in ZIF(ZnCo-3:7)-650N_2, ~0.195±0.006 (~3.08%) in ZIF(ZnCo-5:5)-650N_2 and ~0.789±0.012 (~1.52%) in ZIF(ZnCo-7:3)-650N_2. It indicates that ZIF(ZnCo-3:7)-650N_2 has the moderate amounts of Co_3ZnC.

As it is known, Zn is a volatile metal at relatively higher temperatures (> 420 °C, i.e., the melting point), which is easy to escape from the ZIF(ZnCo) precursors during the pyrolysis at a temperature beyond melting point [*Adv. Funct. Mater.*, 2017, **27**, 1700795.]. Thus, the results above may be a competition between the formation of Co_3ZnC and the volatilization of Zn, which is similar to the reported findings by Xiao,

et al. [*ACS Nano*, 2014, **8**, 7846-7857.]. A temperature within 600-700 °C is favourable for the formation of Co_3ZnC [*ACS Nano*, 2014, **8**, 7846-7857; *ACS Appl. Mater. Interfaces*, 2018, **10**, 6245-6252; *J. Catal.*, 2021, **401**, 17-26; *ACS Appl. Mater. Interfaces*, 2016, **8**, 26834-26841.]. The lower temperatures have insufficient thermal energy to drive the formation, while the higher ones accelerate the volatilization of Zn. Thus, the pyrolysis temperature of 650 °C benefits the formation of Co_3ZnC. Furthermore, the results above (Figs. 1 and S2) suggest that the fed molar ratios of Zn:Co also influence the formation of Co_3ZnC. A small fed Zn in the ZIF(ZnCo-1:9) is not enough to form Co_3ZnC. When the more fed Zn is provided, Co_3ZnC begins to form in ZIF(ZnCo-3:7)-650N_2, ZIF(ZnCo-5:5)-650N_2 and ZIF(ZnCo-7:3)-650N_2. However, it is still difficult for the current results to figure out why the weight or molar ratios of Co_3ZnC:fcc Co do not gradually follow the fed molar ratios of Zn:Co. It may also be the competitive results between the formation of Co_3ZnC and the volatilization of Zn, which needs further detailed investigations.
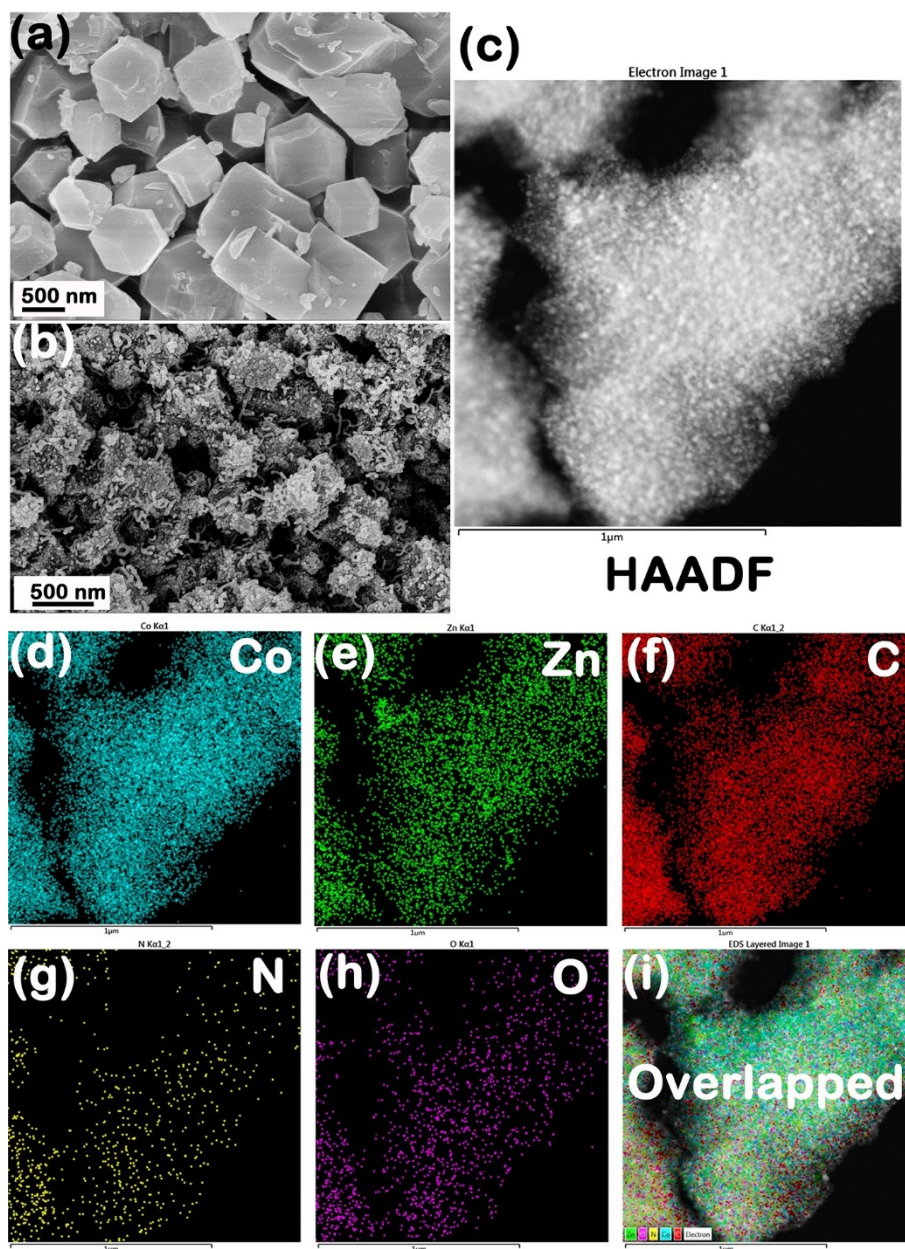
Fig. S3 SEM images of (a) ZIF(ZnCo-3:7) and (b) ZIF(ZnCo-3:7)-650N$_2$. (c) High-angle annular dark field (HAADF) image. (d)-(h) Energy dispersive spectroscopy (EDS) mapping images for Co, Zn, C, N and O, respectively. (i) Overlapped images of (c)-(h).
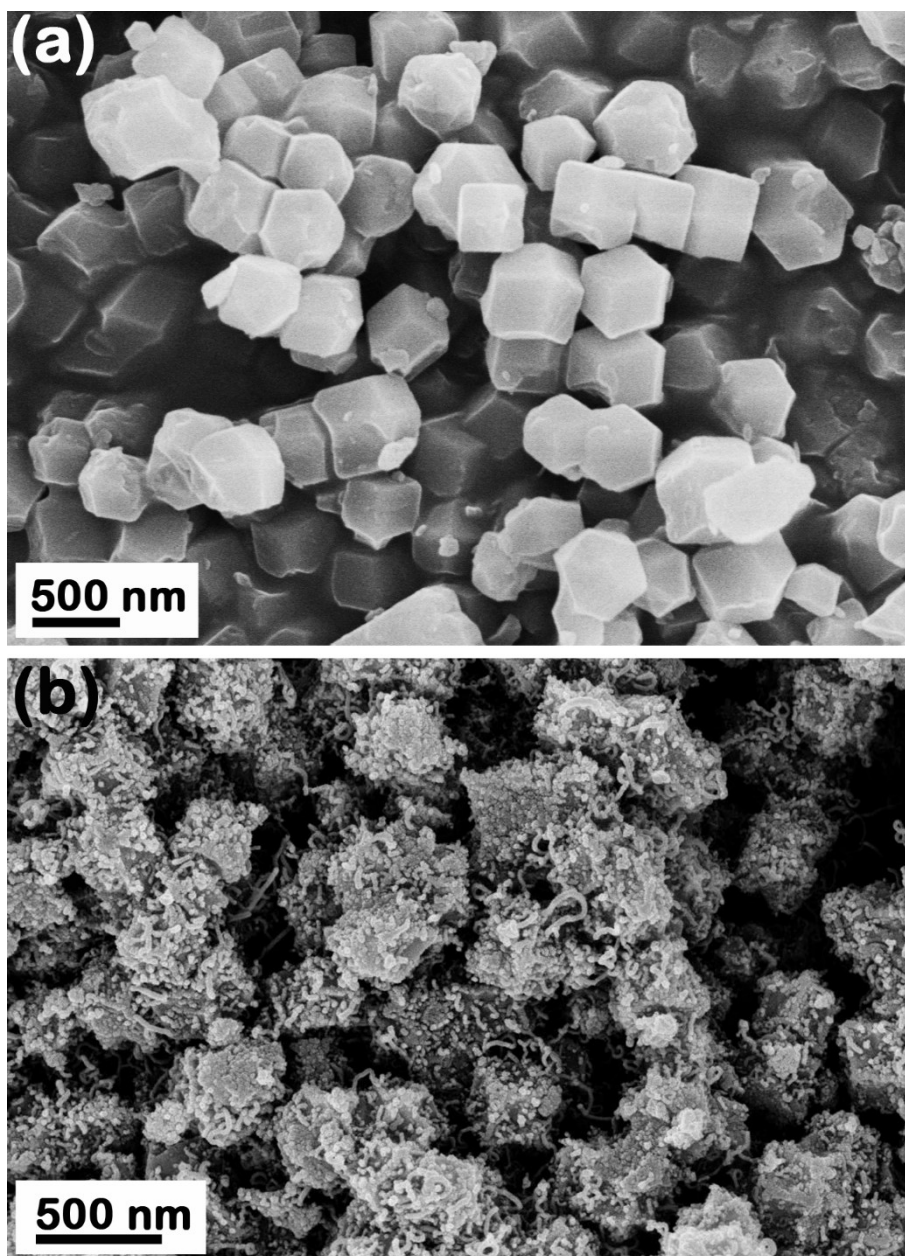
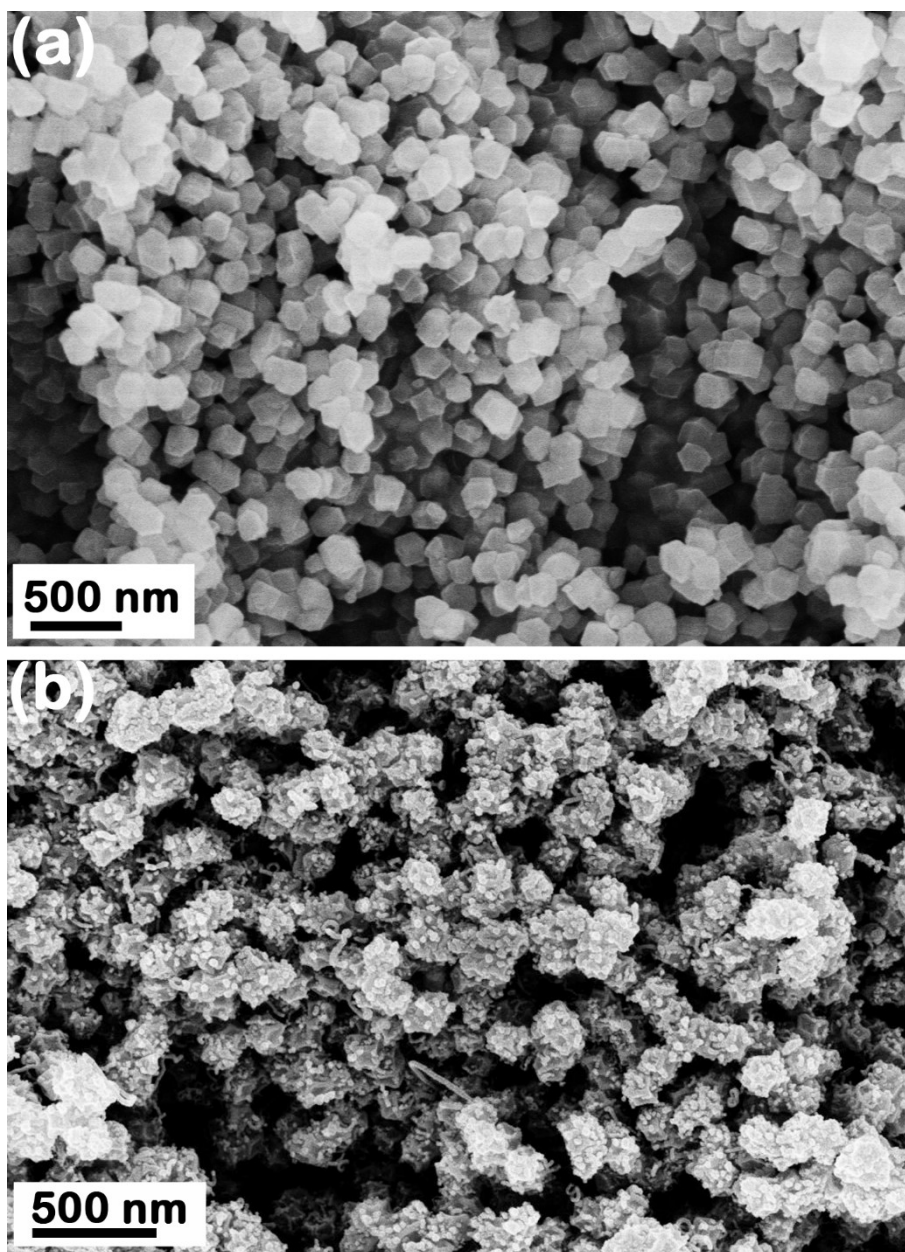**Fig. S4** SEM images of (a) ZIF(ZnCo-5:5) and (b) ZIF(ZnCo-5:5)-650N$_2$.

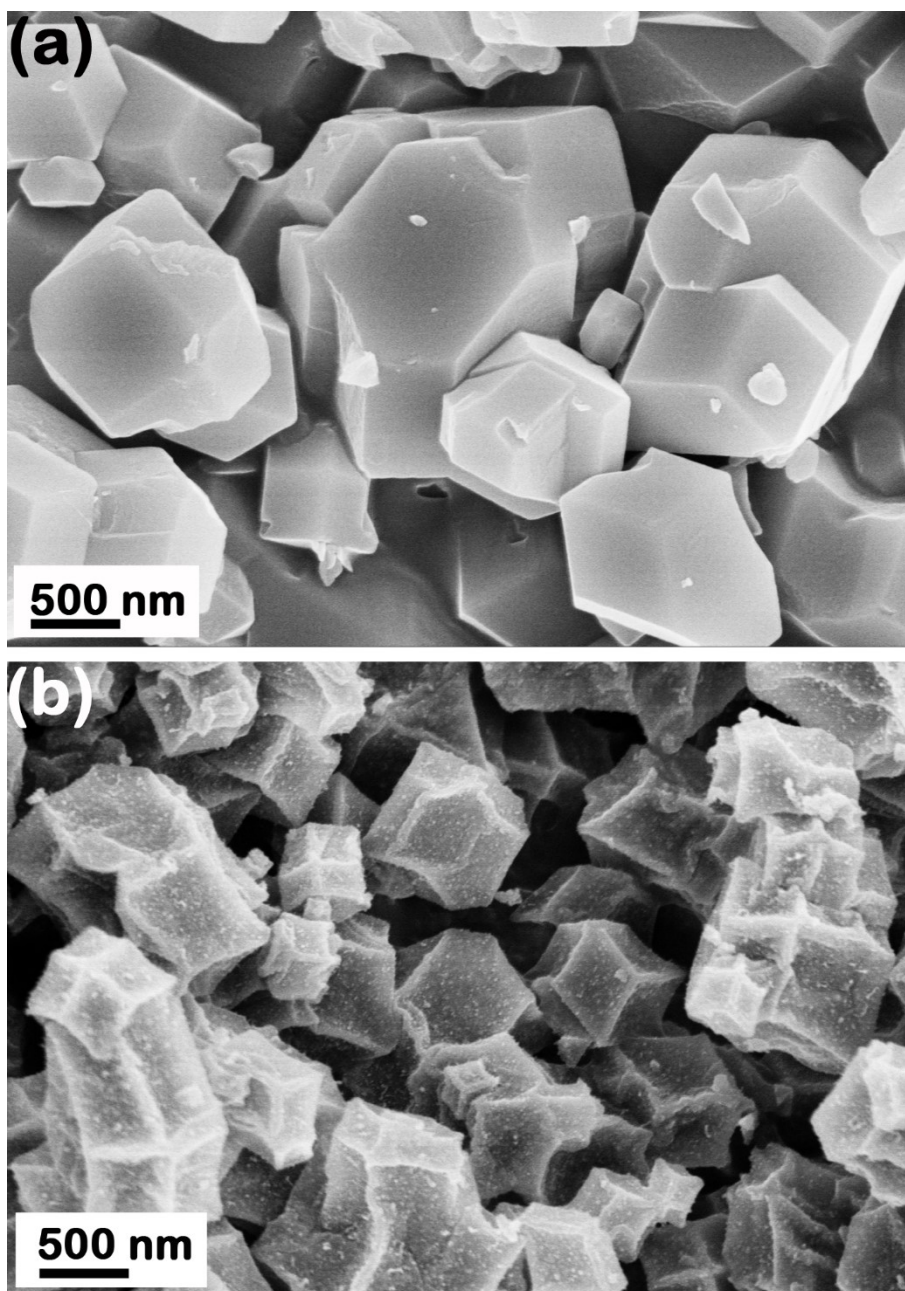**Fig. S5** SEM images of (a) ZIF(ZnCo-7:3) and (b) ZIF(ZnCo-7:3)-650N$_2$.

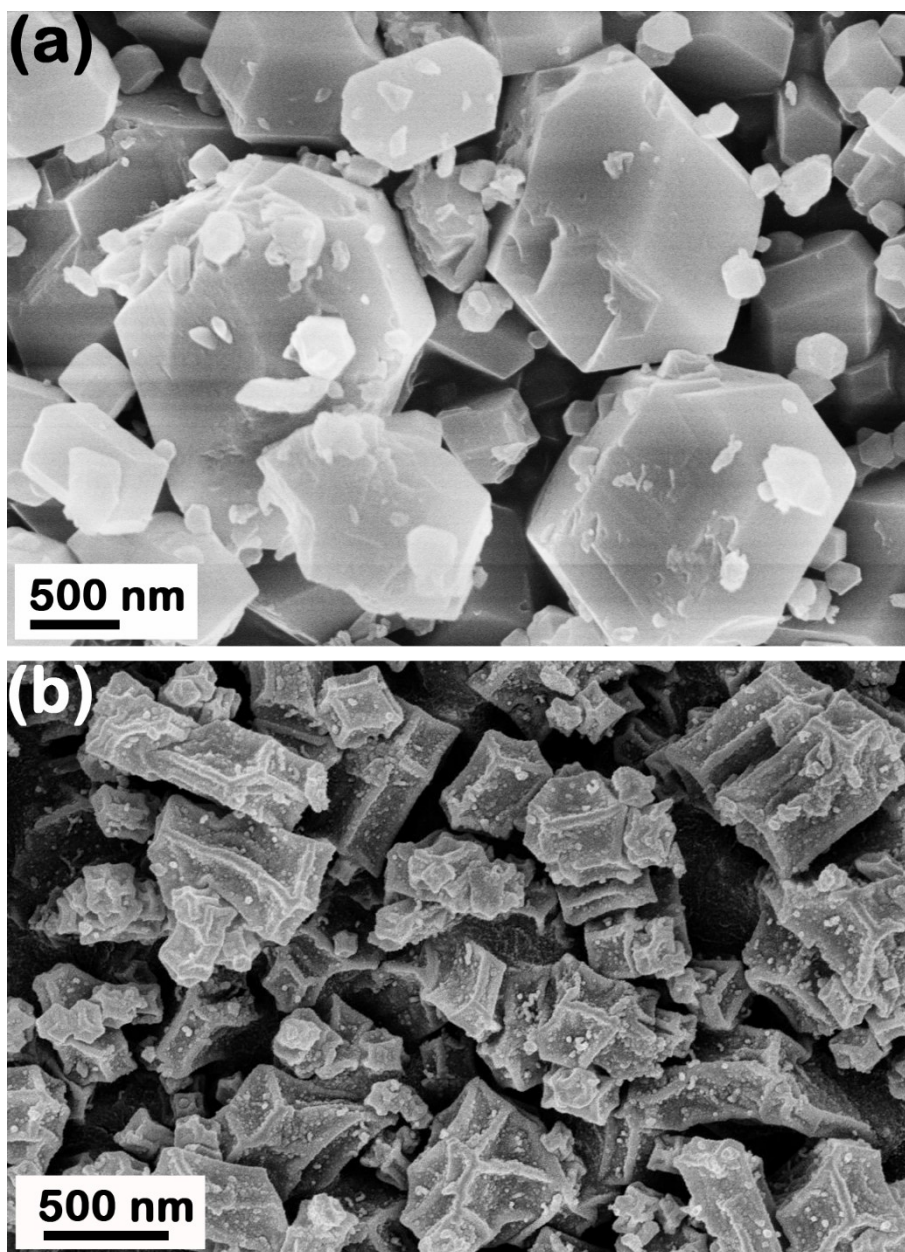**Fig. S6** SEM images of (a) ZIF(ZnCo-1:9) and (b) ZIF(ZnCo-1:9)-650N$_2$.

Fig. S7 SEM images of (a) ZIF-67 and (b) ZIF-67-650N$_2$.
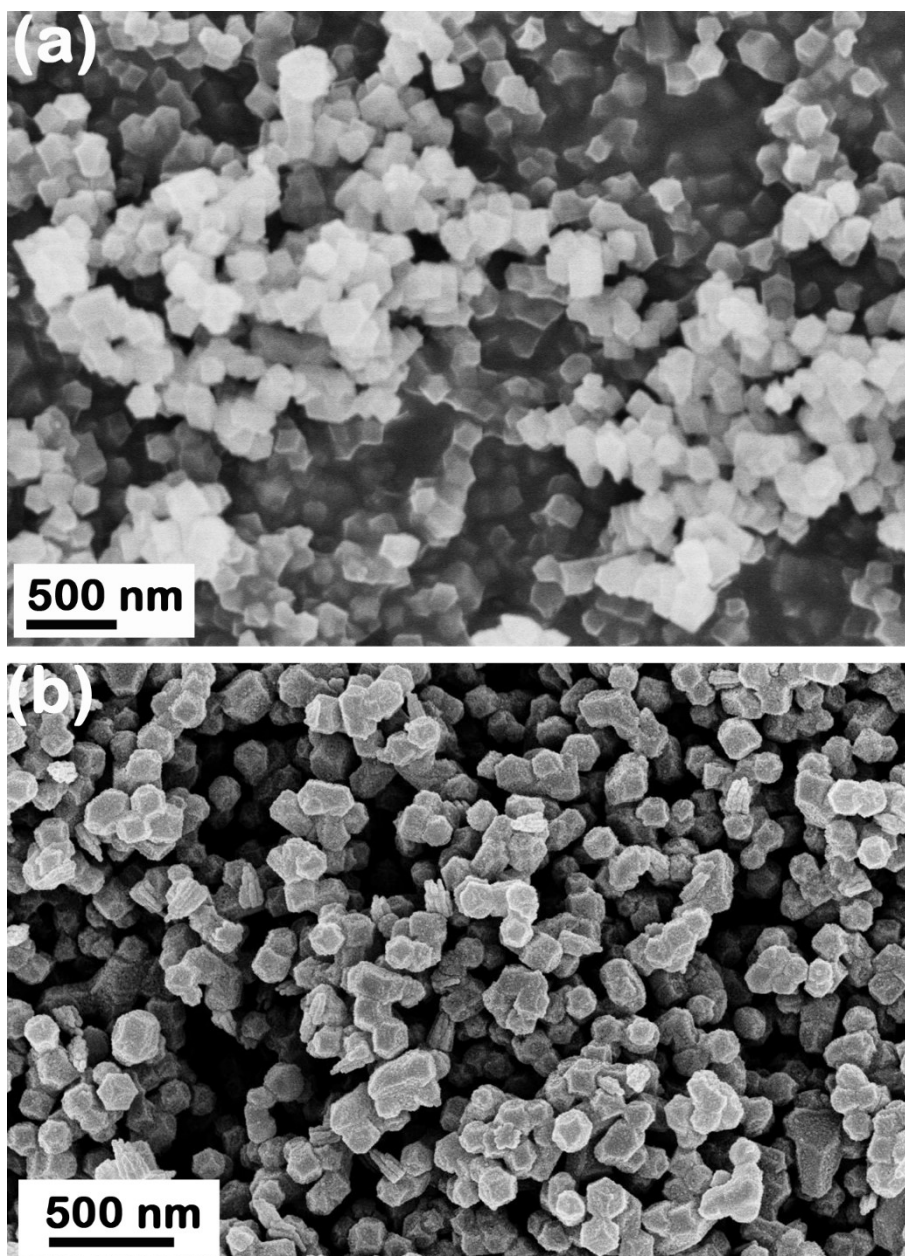
Fig. S8 SEM images of (a) ZIF-8 and (b) ZIF-8-650N$_2$.

Fig. S9 (a) TEM and (b) HRTEM images of ZIF(ZnCo-5:5)-650N$_2$. (c) High-angle annular dark field (HAADF) image. (d) The overlapped mapping images of Co, Zn, C, N and O. (e)-(i) The separate EDS mapping images for Co, Zn, C, N and O, respectively.

Fig. S10 (a) TEM and (b) HRTEM images of ZIF(ZnCo-7:3)-650N$_2$. (c) High-angle annular dark field (HAADF) image. (d) The overlapped mapping images of Co, Zn, C, N and O. (e)-(i) The separate EDS mapping images for Co, Zn, C, N and O, respectively.
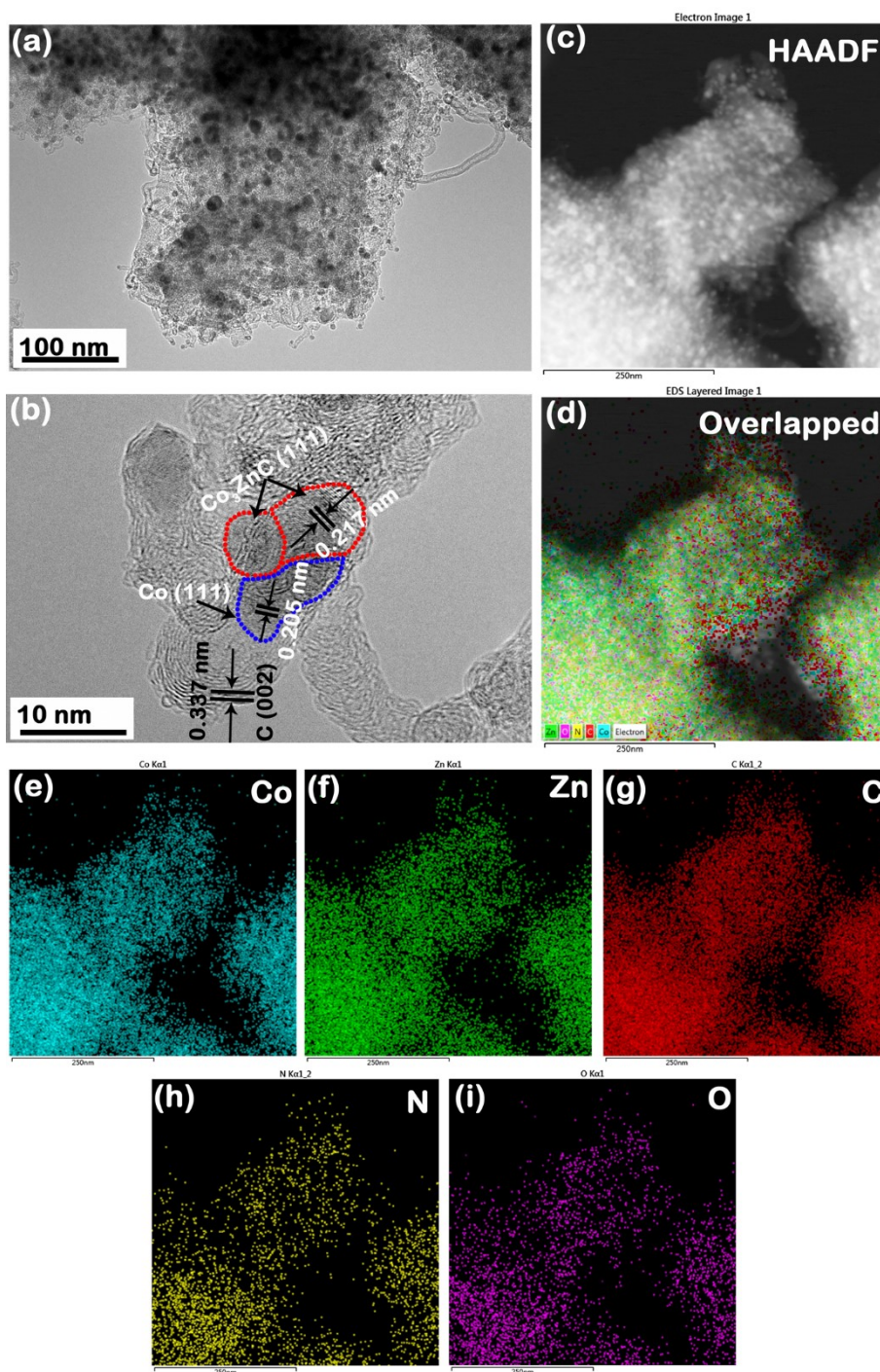
Fig. S11 (a) TEM and (b) HRTEM images of ZIF(ZnCo-1:9)-650N$_2$. (c) High-angle annular dark field (HAADF) image. (d) The overlapped mapping images of Co, Zn, C, N and O. (e)-(i) The separate EDS mapping images for Co, Zn, C, N and O, respectively.
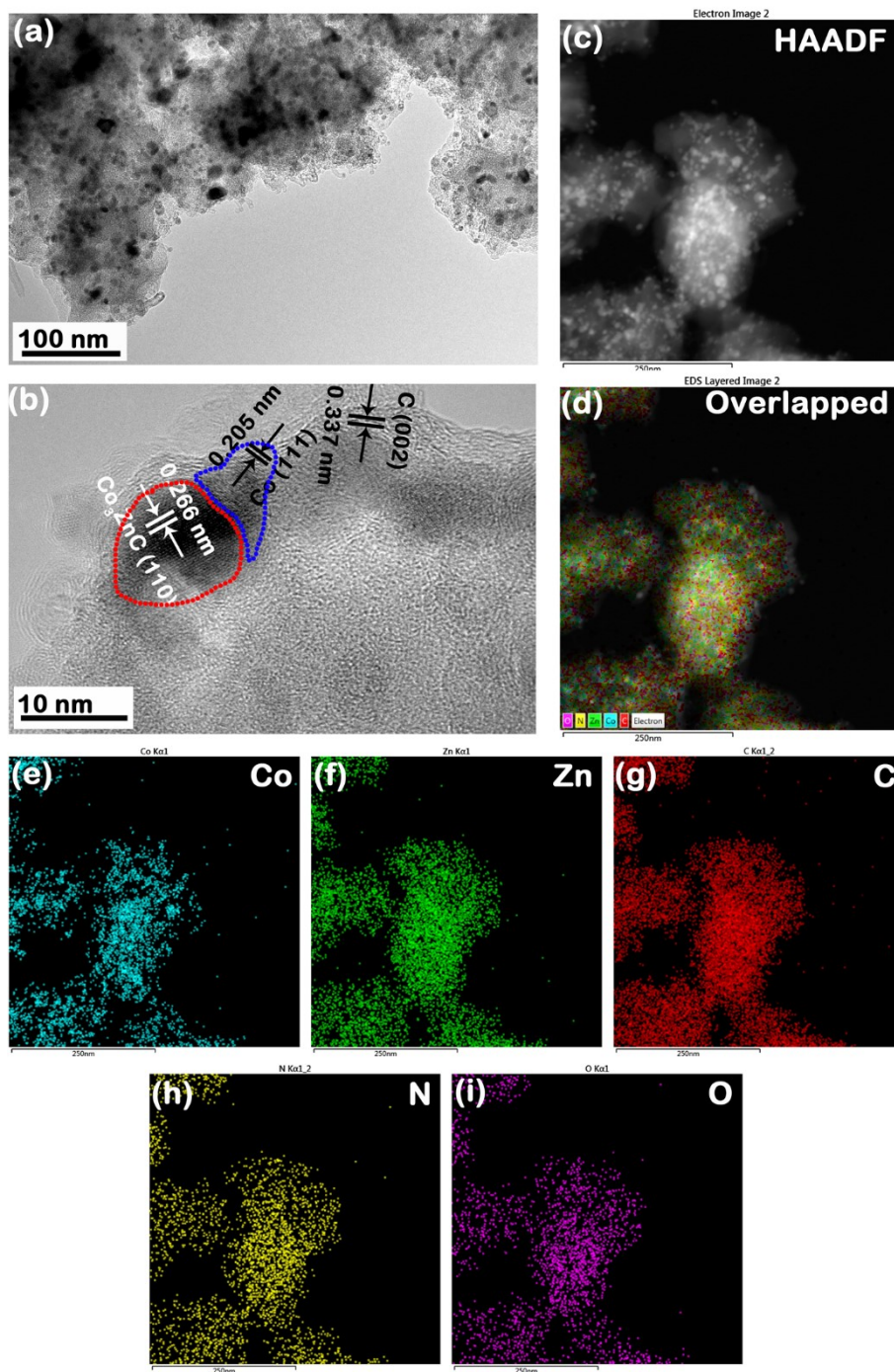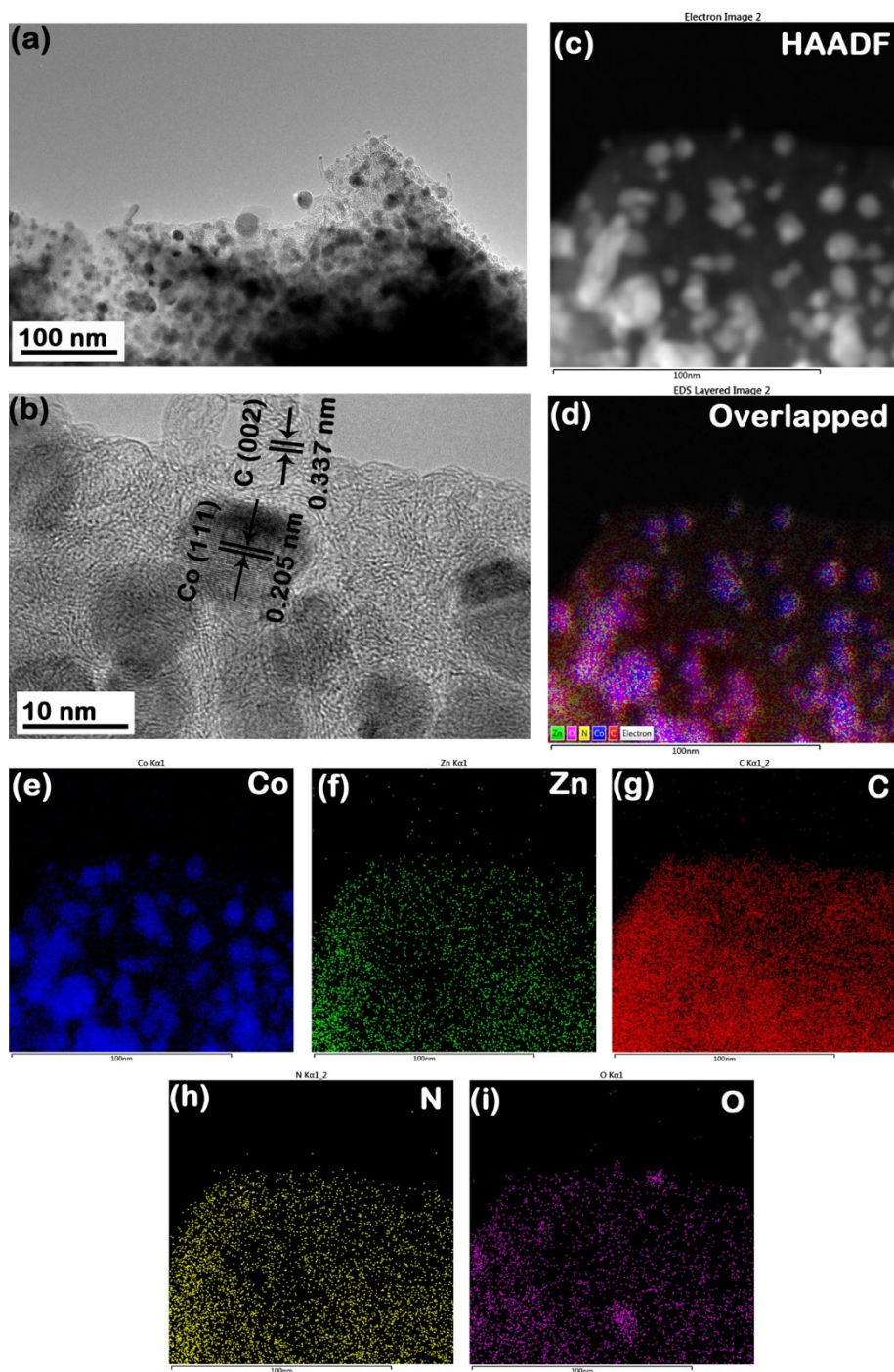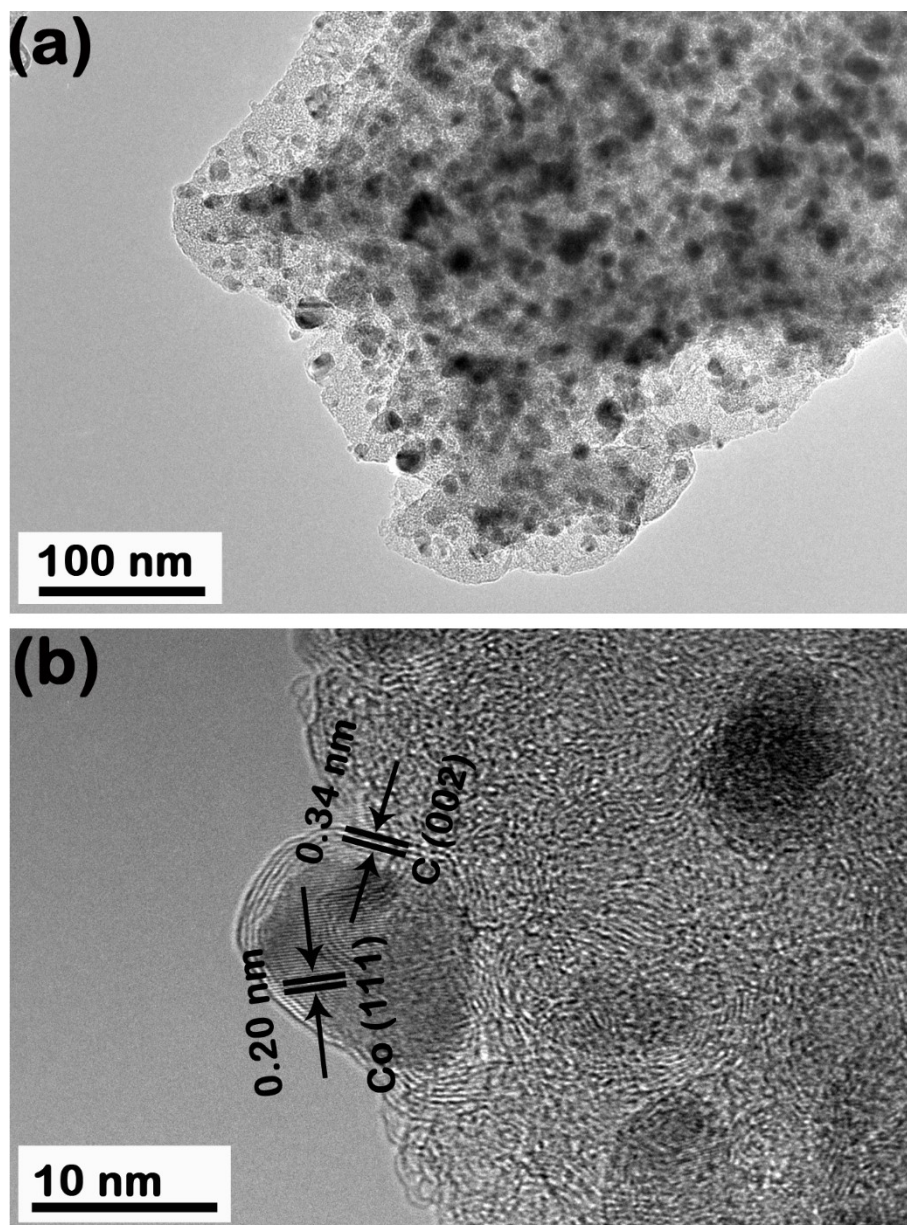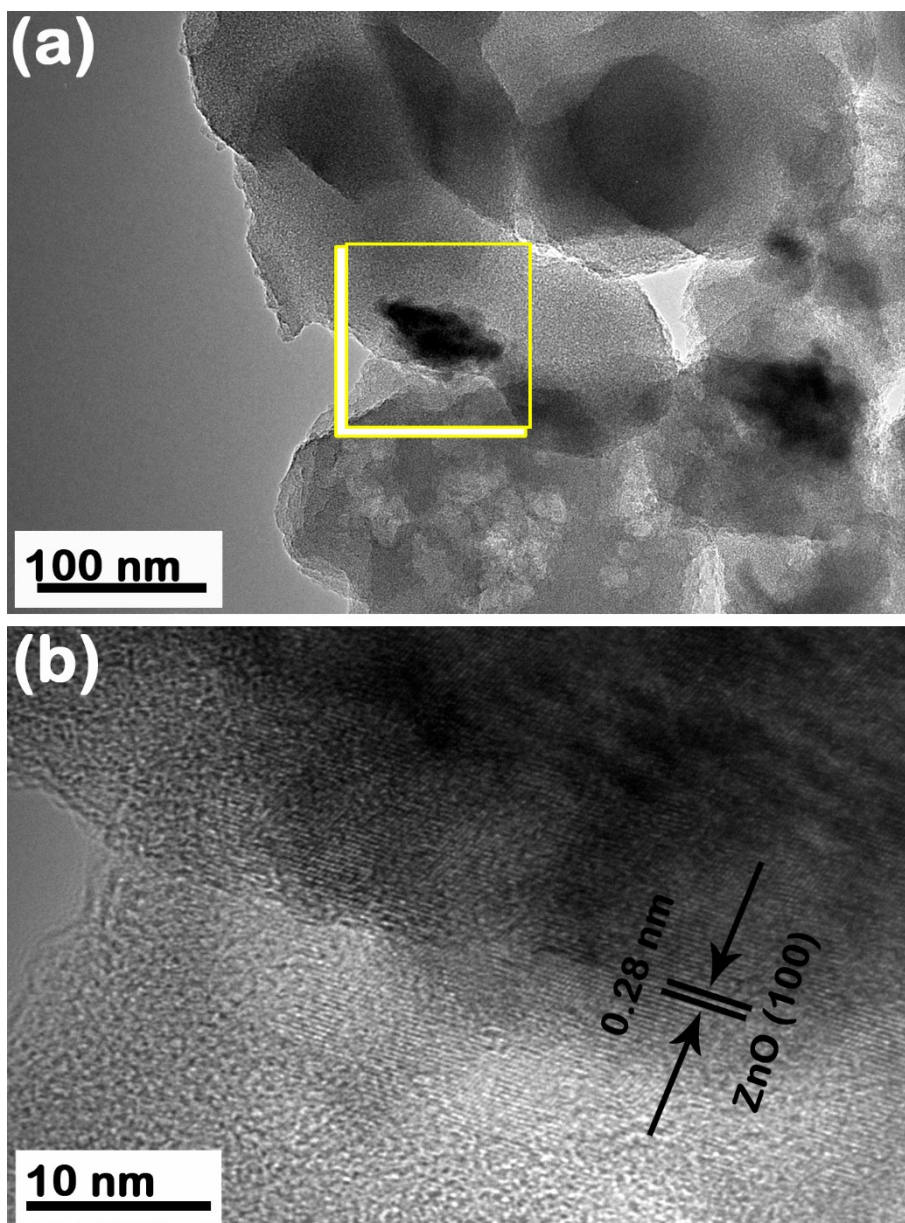
Fig. S12 (a) TEM and (b) HRTEM images of ZIF-67-650N$_2$.
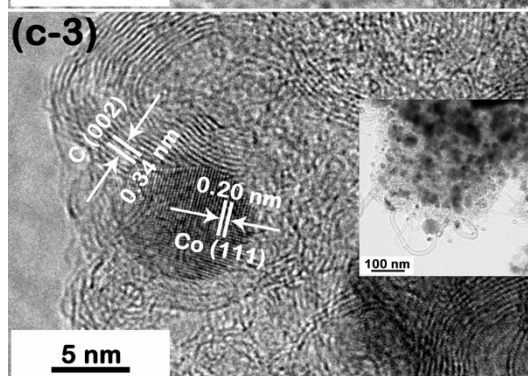
Fig. S13 (a) TEM and (b) HRTEM images of ZIF-8-650N$_2$.
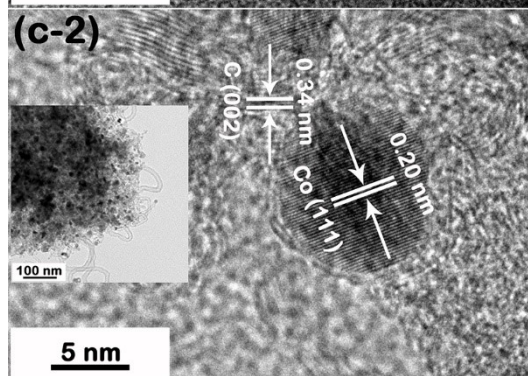
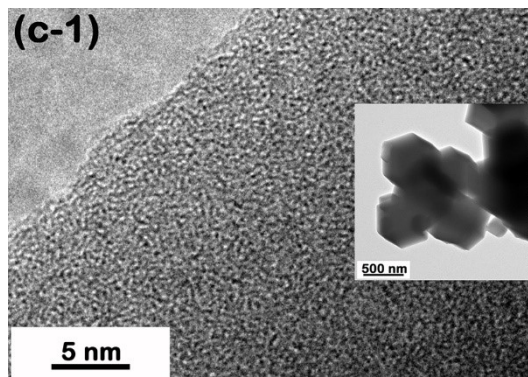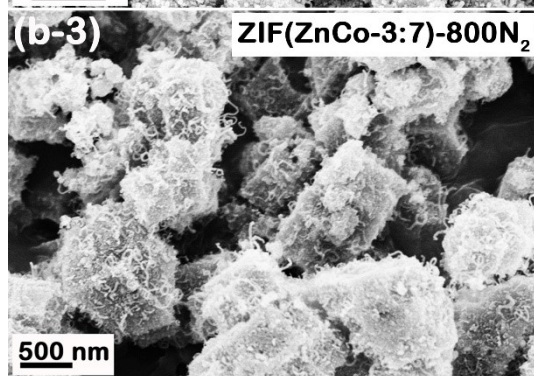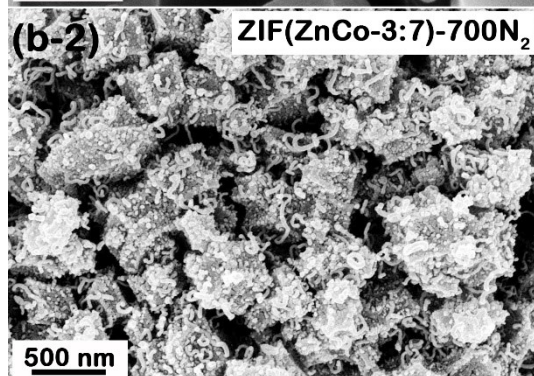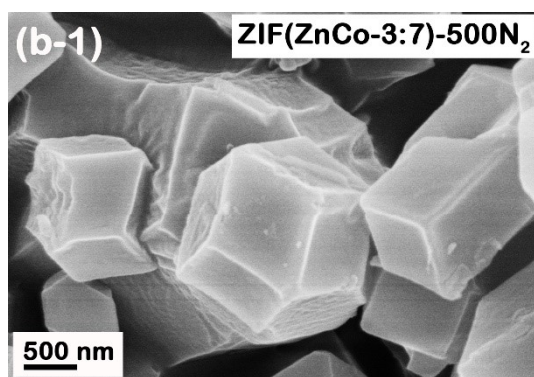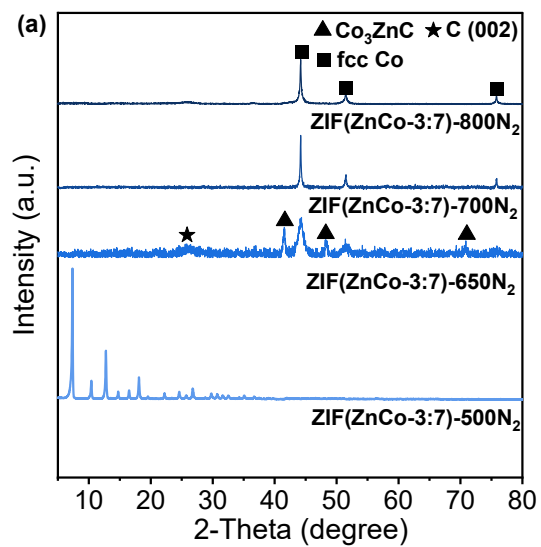**Fig. S14** (a) XRD patterns of the samples prepared at different pyrolysis temperatures. (b) Corresponding SEM images. (c) Corresponding (HR)TEM images, (c-1) for ZIF(Zn:Co-3:7)-500N_2, (c-2) for ZIF(Zn:Co-3:7)-700N_2 and (c-3) for ZIF(Zn:Co-3:7)-800N_2.

Note S2 As shown in Fig. S14a, a pyrolysis temperature at 500 ^oC is insufficient to decompose ZIF(Zn:Co-3:7) effectively, and its XRD pattern well agrees with that for ZIF(Zn:Co-3:7) in Fig. S1. When the temperatures are beyond 650 ^oC, such as 700 and 800 ^oC, they are high enough to make Zn volatilize easily [*Adv. Funct. Mater.*, 2017, 27, 1700795.], leaving only fcc Co and carbons in the resultant ZIF(Zn:Co-3:7)-700N_2 and -800N_2. Thus, moderate temperatures (herein, 650 ^oC) are required to be favourable for the formation of Co$_3$ZnC (Fig. 1). The observation is consistent with the reported works [*J. Mater. Chem. A*, 2016, **4**, 9204-9212. *ACS Appl. Mater. Interfaces*, 2018, **10**, 6245. *J. Mater. Chem. A*, 2015, **3**, 11066-11073. *ACS Appl. Mater. Interfaces*, 2022, **14**, 41246–41256.].

Fig. S14(b-1) shows the SEM image of ZIF(Zn:Co-3:7)-500N_2. The general morphology of ZIF(Zn:Co-3:7)-500N_2 is similar to that of ZIF(Zn:Co-3:7) (Fig. S3a), which agrees with the XRD results above (Fig. S14a). Even so, the surfaces of rhombic dodecahedrons in ZIF(Zn:Co-3:7)-500N_2 shrink to a certain extent and become rougher as compared with those in ZIF(Zn:Co-3:7). When the pyrolysis temperature rises to 650 ^oC, the framework of ZIF(Zn:Co-3:7) decomposes significantly and many CNTs grow on the surfaces of rhombic dodecahedrons (Fig. 2). The similar surface morphologies of rhombic dodecahedrons are observed in ZIF(Zn:Co-3:7)-700N_2 (Fig.

S14(b-2)) and -800N$_2$ (Fig. S14(b-3)). The detailed nanostructures can be observed in their TEM and HRTEM images (Figs. S14(c-1)-(c-3)). As shown in the inset of Fig. S14(c-1), ZIF(Zn:Co-3:7)-500N$_2$ well keeps the morphology of rhombic dodecahedron, which is consistent with the SEM result above (Fig. S14(b-1)), and its HRTEM image show that there are no nanoparticles and surrounding carbon layers observed at 500 ^{o}C. The degree of pyrolysis increases along with the raised temperatures, which results in the different nanostructures. For a pyrolysis temperature at 650 ^{o}C, ZIF(Zn:Co-3:7)-650N$_2$ is composed of Co$_3$ZnC-Co hybrid wrapped with graphitized carbon layers and CNTs grown out of carbon matrices (Fig. 2). When the higher pyrolysis temperatures are beyond 650 ^{o}C (i.e., 700 and 800 ^{o}C), ZIF(Zn:Co-3:7)-700N$_2$ and -800N$_2$ hardly have Co$_3$ZnC. Co nanoparticles and their surrounding graphitized carbon layers as well as CNTs constitute their similar nanostructures (Fig. S14(c-2) for ZIF(Zn:Co-3:7)-700N$_2$ and Fig. S14(c-2) for ZIF(Zn:Co-3:7)-800N$_2$).
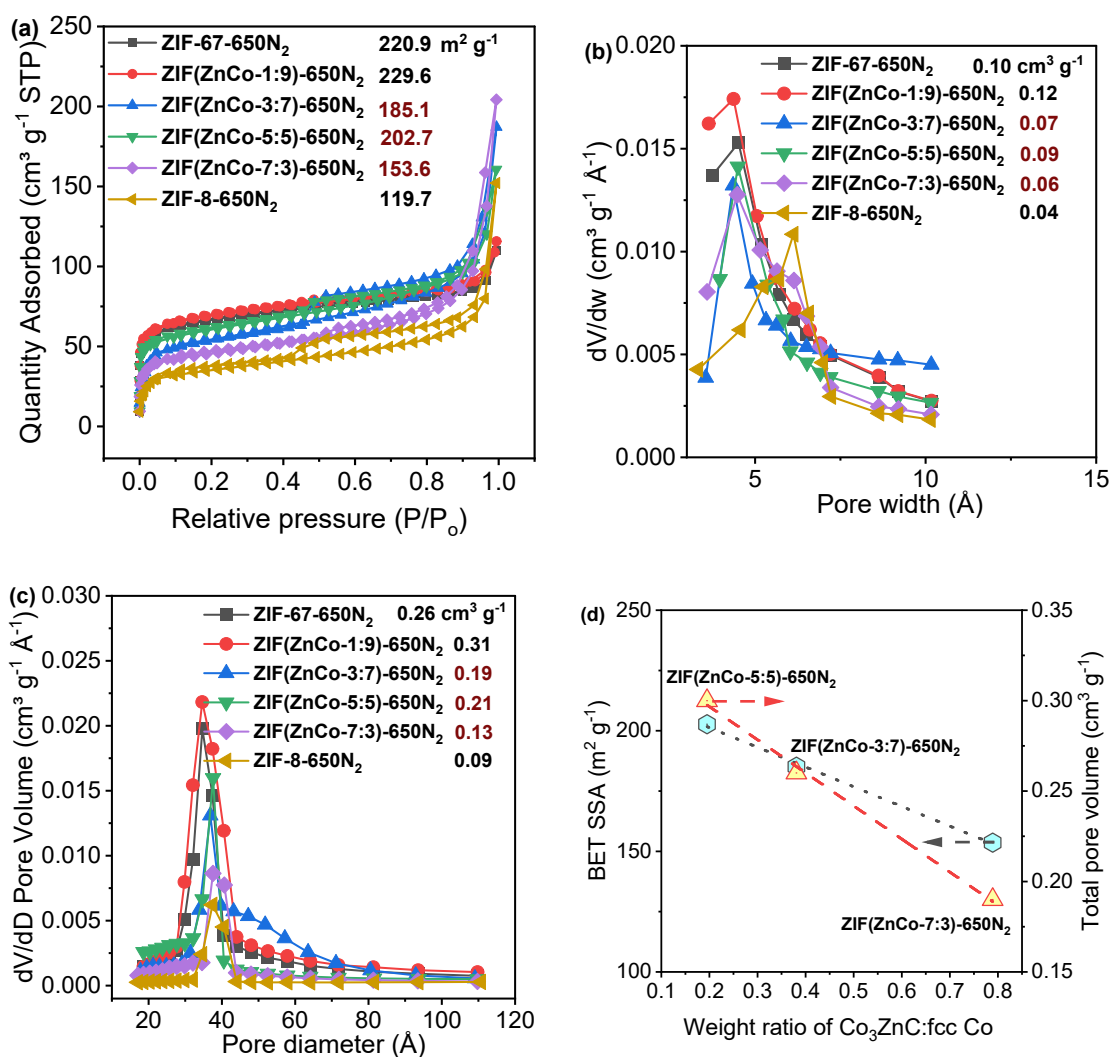
Fig. S15 (a) N₂-sorption isotherms at 77 K. (b) Micropore size distributions. (c) Mesopore size distributions. (d) Relationships of BET SSAs and total pore volumes with weight ratio of Co₃ZnC:fcc Co.

Note S3 All the resultant catalysts prepared at 650 °C have Type VIa N₂-sorption isotherms and Type H4 hysteresis loops (Fig. S15a), suggesting there are both micropores and mesopores [*Pure Appl. Chem.*, 2015, **87**, 1051–1069.]. The micropore distributions (Fig. S15b) are determined by Horvath-Kawazoe (HK) method, while the mesopore distributions (Fig. S15c) are analyzed from Barret-Joyner-Halenda (BJH)

desorption branches. For micropores, the sizes of all the resultant catalysts are concentrated at ~4.5 Å except for ZIF-8-650N$_2$ (~6.1 Å), while their mesopores have the concentrated sizes of ~36 Å. According to the XRD results (Fig. 1) and the further SEM and TEM results (Figs. 2 and S3-S13), ZIF-67-650N$_2$ and ZIF(ZnCo-1:9)-650N$_2$ are composed of fcc Co and carbons (with high graphitization degree); ZIF(ZnCo-3:7)-650N$_2$, ZIF(ZnCo-5:5)-650N$_2$, and ZIF(ZnCo-7:3)-650N$_2$ have Co$_3$ZnC, fcc Co and carbons (with high graphitization degree); and ZIF-8-650N$_2$ is consisted of ZnO and carbons (with low graphitization degree). Thus, the resultant catalysts at 650 ^{o}C are divided into three groups. Group-1 includes ZIF-67-650N$_2$ and ZIF(ZnCo-1:9)-650N$_2$, Group-2 contains ZIF(ZnCo-3:7)-650N$_2$, ZIF(ZnCo-5:5)-650N$_2$, and ZIF(ZnCo-7:3)-650N$_2$, and only ZIF-8-650N$_2$ constitutes Group-3. For Group-1, Zn with small amounts in ZIF(ZnCo-1:9) precursor is favourable for slightly higher BET specific surface area (SSA) (Fig. S15a) and larger micropore (Fig. S15b) and mesopore (Fig. S15c) volumes for the resultant ZIF(ZnCo-1:9)-650N$_2$, which should be attributed to the evaporation of Zn during pyrolysis [*Adv. Funct. Mater.*, 2017, **27**, 1700795. *Adv. Mater.*, 2022, **34**, 2107072.]. Further, Group-2 with Co$_3$ZnC generally have the lower BET SSAs and smaller micropore and mesopore volumes as compared with Group-1 without it. Notably, the BET SSAs and total pore volumes (adding micropore and mesopore volumes together) decrease linearly with the weight ratios of Co$_3$ZnC:fcc Co (Fig. S15d). The results above indicate that Co$_3$ZnC exerts negative effects on BET SSAs and pore volumes. In addition, for Group-3, ZIF-8-650N$_2$ has the lowest BET SSA and smallest micropore and mesopore volumes, which is mainly due to carbons with

low graphitization degree as well as ZnO.
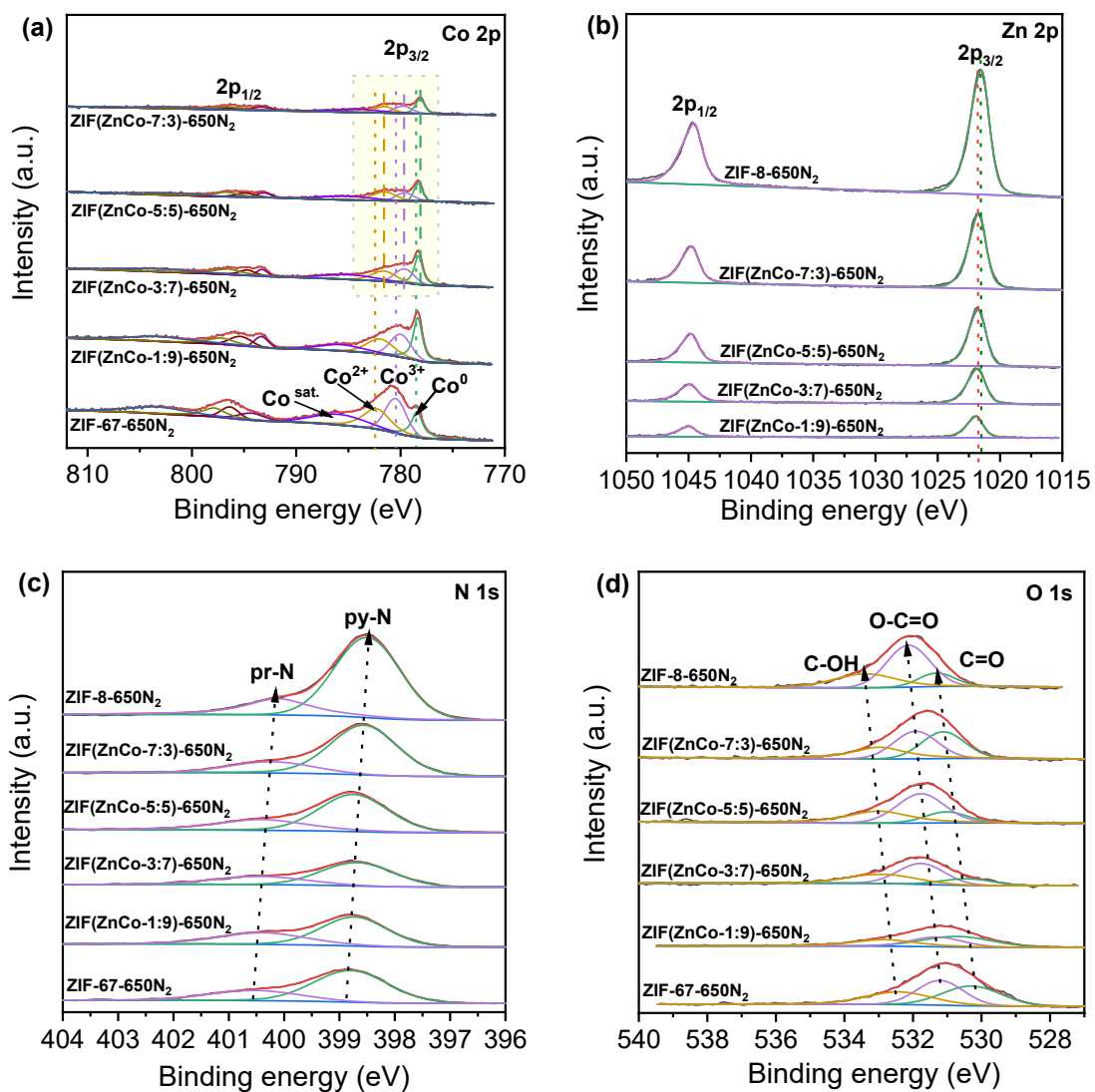
Fig. S16 XPS spectra of the resultant catalysts: (a) Co 2p. (b) Zn 2p. (d) N 1s. (e) O 1s.
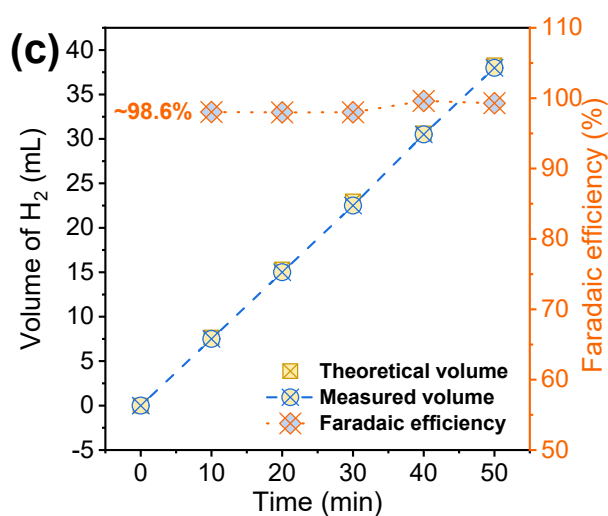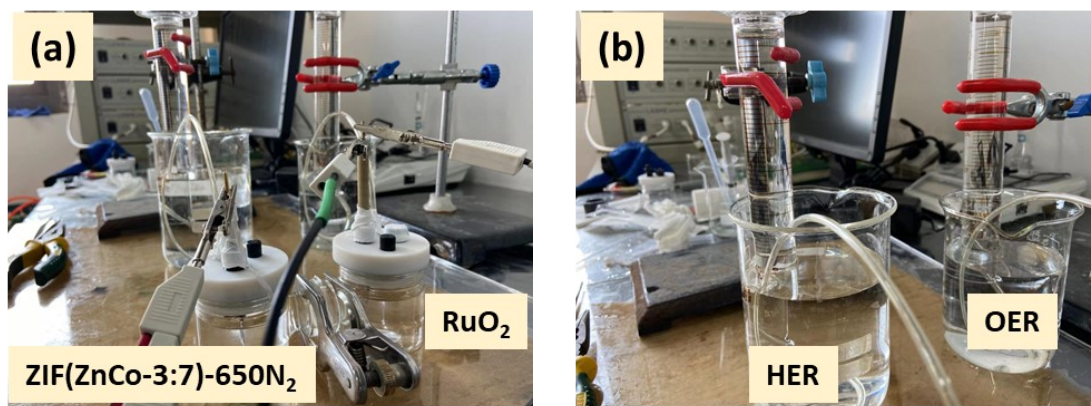
Fig. S17 (a) Photograph of water–gas displacing system with two electrodes. (b) Photograph of H_2 and O_2 collections. (c) Volumes (both theoretical and measured) of H_2 and corresponding Faradaic efficiencies versus running time.

Note S4 A water–gas displacing method was used to detect HER Faradaic efficiency for the optimal ZIF(ZnCo-3:7)-650N$_2$ [*ACS Appl. Mater. Interfaces*, 2022, **14**, 27842–27853. *Carbon Energy*, 2022, DOI: 10.1002/cey2.273]. The test system consisted of two electrodes (Fig. S17a), i.e., cathode loaded with ZIF(ZnCo-3:7)-650N$_2$ and anode loaded with RuO_2 as benchmarked catalyst toward oxygen evolution. Both loading of ZIF(ZnCo-3:7)-650N$_2$ and RuO_2 on carbon paper was ~0.5 mg cm^{-2}. To separate two

chambers, a treated Nafion-117 membrane was used [*ACS Appl. Mater. Interfaces,*

2020, 12, 19447–19456]. The pristine Nafion-117 membrane (Dupont Company, USA)

was activated in H_2O_2 aqueous solution (5 wt.%) at 80 °C for 1 h, and then heated in

ultrapure water at 80 °C for 1 h, and then washed with ultrapure water several times

to remove residual H_2O_2, and finally stored in ultrapure water before it was used.

After the test system was constructed, overall water splitting was performed at a

constant current of 100 mA for 50 min. Meanwhile, H_2 produced at the cathode was

collected and measured by displacing water in a measuring cylinder (Fig. S17b).

The measured volume of H_2 is labelled as V_m. The theoretical volume (V_t) is

calculated by the following equation:

$$V_t = \frac{n_{H_2} RT}{P^0}$$

(S1)

where R is gas constant (8.314 J mol^{-1} K^{-1}), T is testing temperature (300 K), P^0 is

standard atmospheric pressure (101325 Pa), n_{H2} is moles of the produced H_2. The n_{H2}

is determined by [C. Du, L. Yang, F. Yang, G. Cheng, W. Luo, *ACS Catal., 2017, 7,*

4131–4137.]

$$n_{H_2} = \frac{Q}{nF} = \frac{it}{nF}$$

(S2)

where Q is charging quantity, i is applied current (here, 100 mA or 0.1 A), t is running

time (3000 s), n is number of electrons transferred during a HER process (n = 2), F is

Faradaic constant (96485.33 C mol^{-1}). After measuring and calculating, the V_m and V_t

are shown in Fig. S17c. Obviously, V_m and V_t are very close, obtaining a high Faradaic

efficiency (V_m/V_t) of ~98.6% (a mean value).
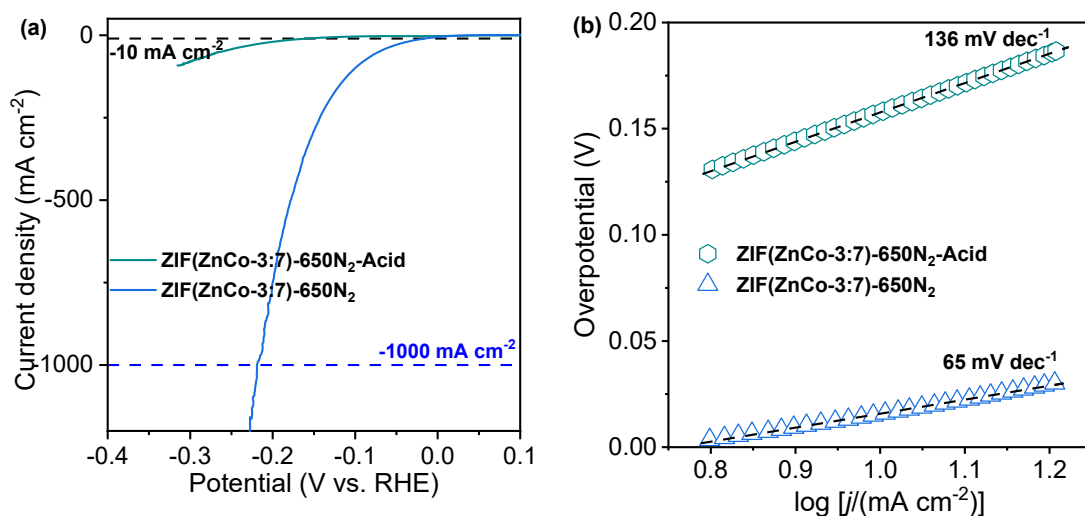
Fig. S18 LSV curves (a) and Tafel slopes (b) of ZIF(ZnCo-3:7)-650N$_2$ in 0.5 M H$_2$SO$_4$ (i.e., ZIF(ZnCo-3:7)-650N$_2$-Acid) and in 1 M KOH (i.e., ZIF(ZnCo-3:7)-650N$_2$).

Note S5 ZIF(ZnCo-3:7)-650N$_2$ has the outstanding HER activity in 1 M KOH, such as a low η_{10} of ~16 mV, a low η_{1000} of ~219 mV, a low Tafel slope of ~65 mV dec^{-1} and a high j_0 of ~5.70 mA cm^{-2}. In sharp contrast, it shows a quite low activity in 0.5 M H$_2$SO$_4$, such as a higher η_{10} of ~138 mV, a higher Tafel slope of ~136 mV dec^{-1} and a much lower j_0 of ~0.70 mA cm^{-2}. The results indicate that ZIF(ZnCo-3:7)-650N$_2$ is a promising HER catalyst in alkaline electrolyte, but it may be unstable in acidic conditions and afford the much inferior HER activity.
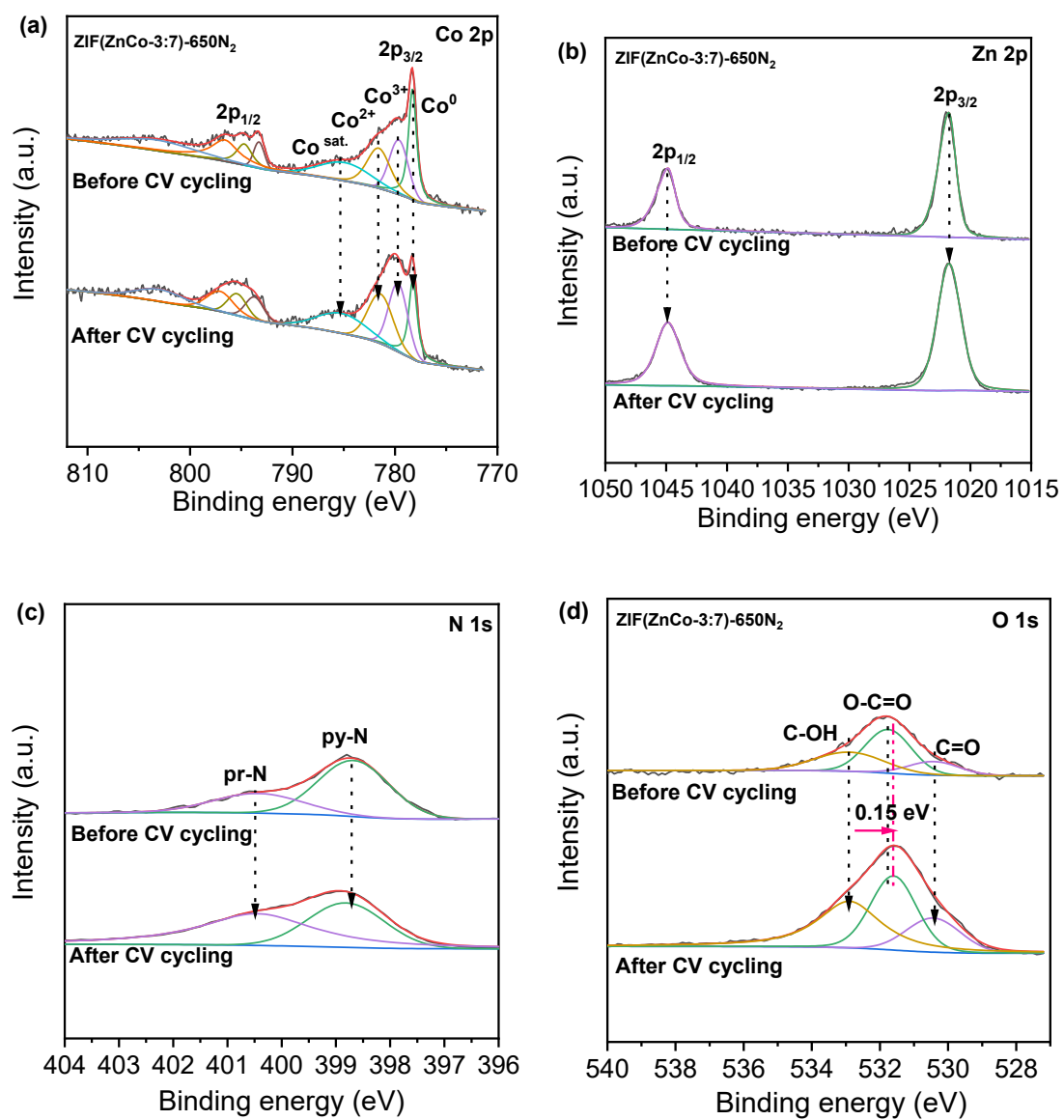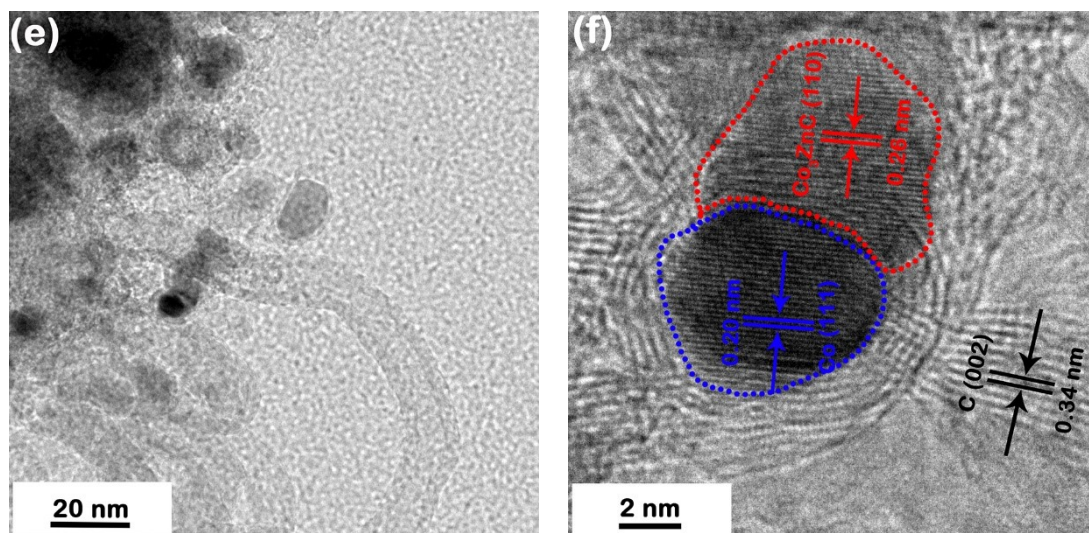
Fig. S19 XPS and TEM results after (before) CV cycling for ZIF(ZnCo-3:7)-650N$_2$: (a) Co 2p XPS spectra. (b) Zn 2p XPS spectra. (c) N 1s XPS spectra. (d) O 1s XPS spectra. (e) TEM image after CV cycling. (f) HRTEM image after CV cycling.

Note S6 As shown in Figs. S19a-S19d, after CV cycling for a long time, the BE values for various surface species, including Co (Co^0, Co^{3+} and Co^{2+}), Zn (Zn^{2+}), N (pr-N and py-N) and O (hydroxy C-OH and ketonic C=O) species, have very slight changes as compared with the ones before CV cycling, except carboxyl O-C=O (downshifted by ~0.15 V as indicated by Fig. S19d). Furthermore, the total surface contents of Co and Zn are close before and after CV cycling, that is, 1.70 vs. 1.68 at%, and 2.30 vs. 2.35 at%. But, the content distributions of those Co species are different after CV cycling, as shown in Table S6. In addition, the total surface content of N slightly decreases from 8.31 to 7.95 at%, whereas that of O increases from 6.83 to 9.27 at%. As indicated in Table S6, the surface contents of various N and O species also differ before and after CV cycling. Furthermore, the general nanostructures of ZIF(ZnCo-3:7)-650N$_2$, including CNTs grown out of carbon matrices (Fig. S19e vs. Fig. 2), Co$_3$ZnC-Co

hybrid and its surrounding graphitized carbon layers (Fig. S19f vs. Fig. 2), are kept well after CV cycling. All in all, the BE of surface species and main nanostructures change little, but the surface contents of specific species (Co, N and O-related species) vary after CV cycling.
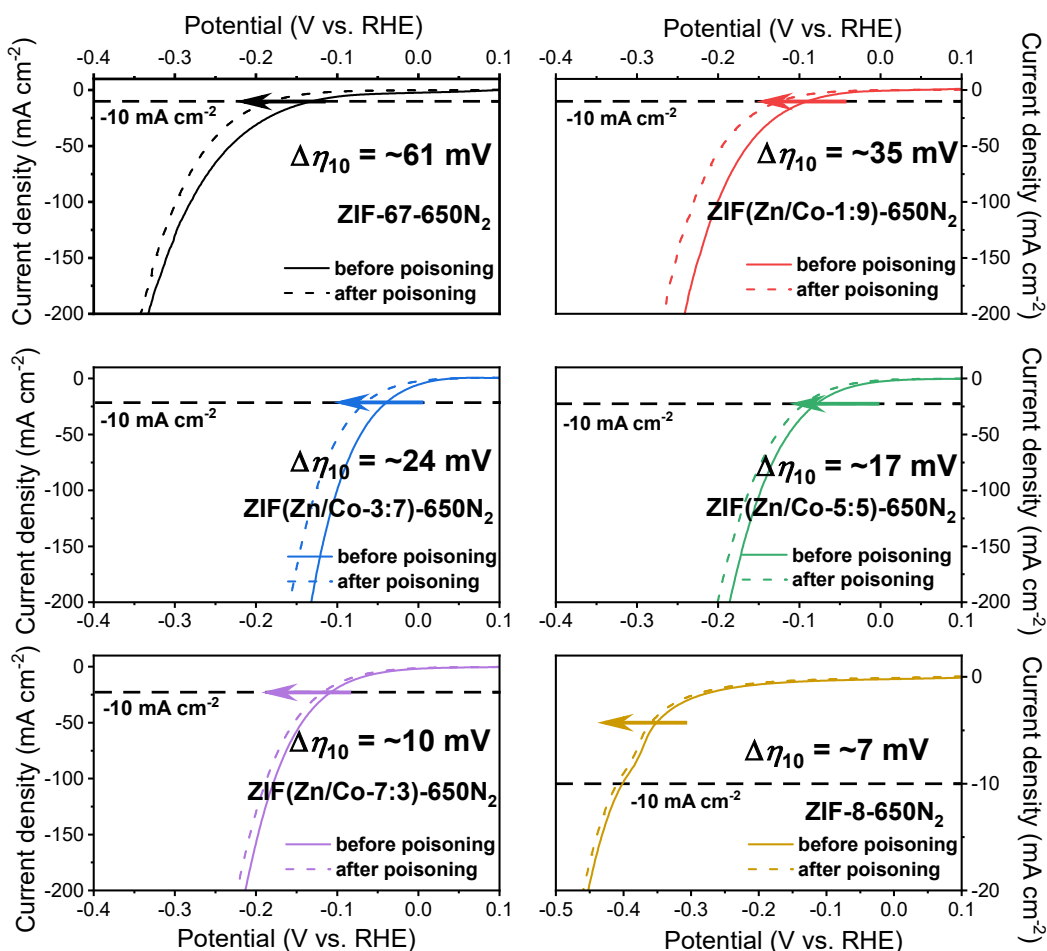
Fig. S20 Poisoning tests in 1 M KOH with 50 mM KSCN for the resultant catalysts.

Note S7 Poisoning tests were used here to investigate possible active species on the surfaces of the resultant catalysts. The LSV curves before and after poisoning are shown in Fig. S20. The $\Delta\eta_{10}$ values decrease with increasing the surface Zn:Co molar ratios. After poisoning, the j_0 values for ZIF-67-650N$_2$, ZIF(ZnCo-1:9)-650N$_2$, ZIF(ZnCo-3:7)-650N$_2$ ZIF(ZnCo-7:3)-650N$_2$, ZIF(ZnCo-5:5)-650N$_2$ and ZIF-8-650N$_2$ have more or less decreases, which are ~0.16, ~0.44, ~2.89, ~1.84, ~1.34 and ~0.06 mA cm^{-2}, respectively. The corresponding j_0 retentions are ~15.2, ~35.2, ~50.7, ~63.2, ~74.1 and ~85.7%, respectively. Apparently, the catalysts with the higher surface Co contents (i.e., the lower surface Zn:Co molar ratios) are more sensitive to SCN$^-$ in

comparison with the ones with the lower surface Co contents (i.e., the higher surface Zn:Co molar ratios). In addition, the doped N species might activate adjacent C atoms as possible active species for HER [*Nat. Energy* 2016, **1**, 16130. *Angew. Chem. Int. Ed.* 2019, **58**, 16217. *Electrochim. Acta* 2020, **334**, 135562.]. However, ZIF-8-650N_2 has the highest surface N content up to ~21.25 at% (Table S2), but has the lowest HER activity among the resultant catalysts. By contrast, the optimal ZIF-ZIF(ZnCo-3:7)-650N_2 only holds the lowest surface N contents (~8.31 at%). Further, ZIF(ZnCo-5:5)-650N_2 and ZIF(ZnCo-7:3)-650N_2 just have the slightly higher surface N contents than ZIF(ZnCo-1:9)-650N_2 and ZIF-67-650N_2, but they afford the significantly enhanced HER activity. The similar correlations between the HER activity and the surface O contents are also observed. What's more, the doped O species in carbons are more unfavourable for HER activity as compared the doped N species based on the reported computational investigations [*Nat. Energy* 2016, **1**, 16130.]. Thus, such results indicate that the doped N and O species fail to provide favourable contributions to HER activity. Therefore, according to the discussion above, it is most likely that the surface Co species serve as the main active sites for HER.
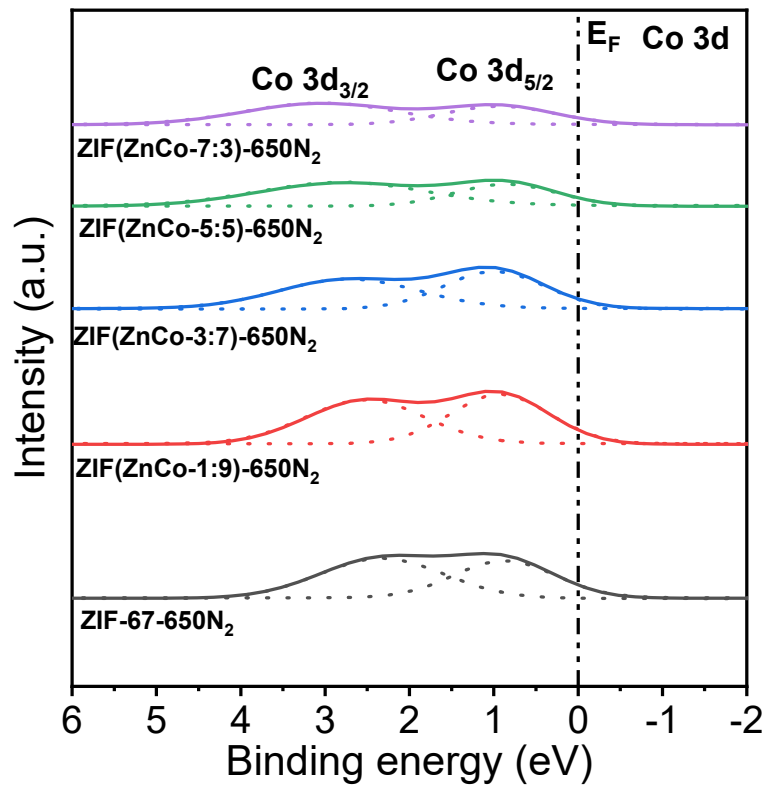
Fig. S21 Co 3d band spectra obtained by subtracting Shirley-type background from the deconvoluted curves of the XPS VB spectra in Fig. 4a.
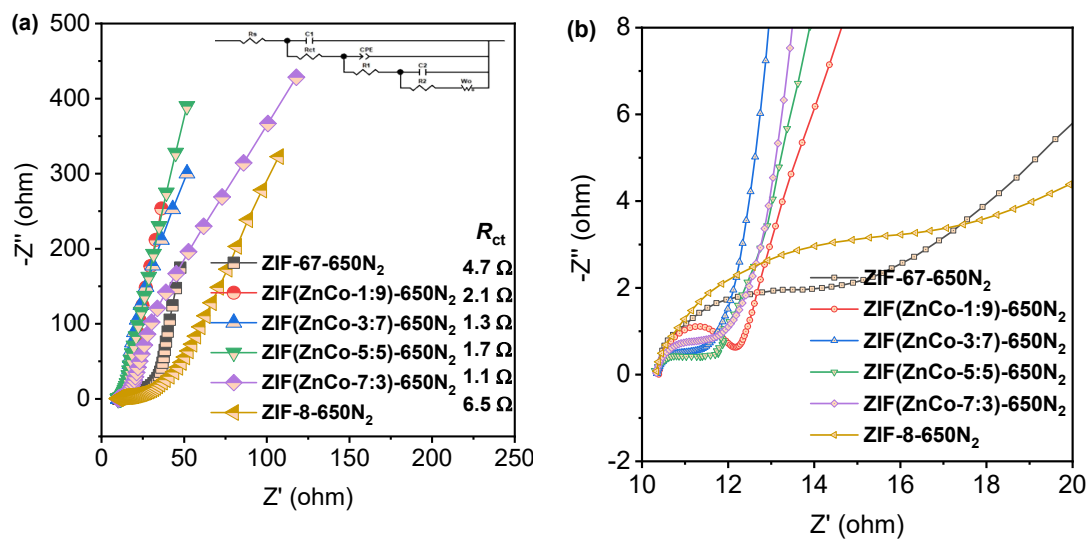
Fig. S22 (a) EIS curves of the resultant catalysts at open circuit potential. (b) Zoomed-in EIS curves within 10-20 Ω of Z'.

Note S8 Fig. S22a and S22b show the EIS curves and the zoomed-in ones within 10-20 Ω of Z', respectively. Charge transfer resistances (R_{ct}) between the electrodes loaded with the resultant catalysts and the electrolytes for ZIF-67-650N$_2$, ZIF(ZnCo-1:9)-650N$_2$, ZIF(ZnCo-3:7)-650N$_2$, ZIF(ZnCo-5:5)-650N$_2$, and ZIF(ZnCo-7:3)-650N$_2$ and ZIF-8-650N$_2$ are ~4.7, ~2.1, ~1.3, ~1.7, ~1.1 and ~6.5 Ω, respectively, as shown in Fig. S17a. The resultant catalysts with Co$_3$ZnC have the similar R_{ct} values. Notably, they are much lower that of the ones without Co$_3$ZnC, which are attributed to Co$_3$ZnC and the concurrently formed CNTs (Fig. 2, and S3-S8, the resultant catalysts with Co$_3$ZnC have both the high contents of Co$_3$ZnC as well as CNTs as compared with the other resultant catalysts). Even though the resultant catalysts with Co$_3$ZnC share the similar R_{ct}, the higher contents of Co$_3$ZnC, the relatively lower R_{ct}. These results suggest that Co$_3$ZnC together with the concurrently formed CNTs can greatly

enhance the charge transfer during the HER processes.
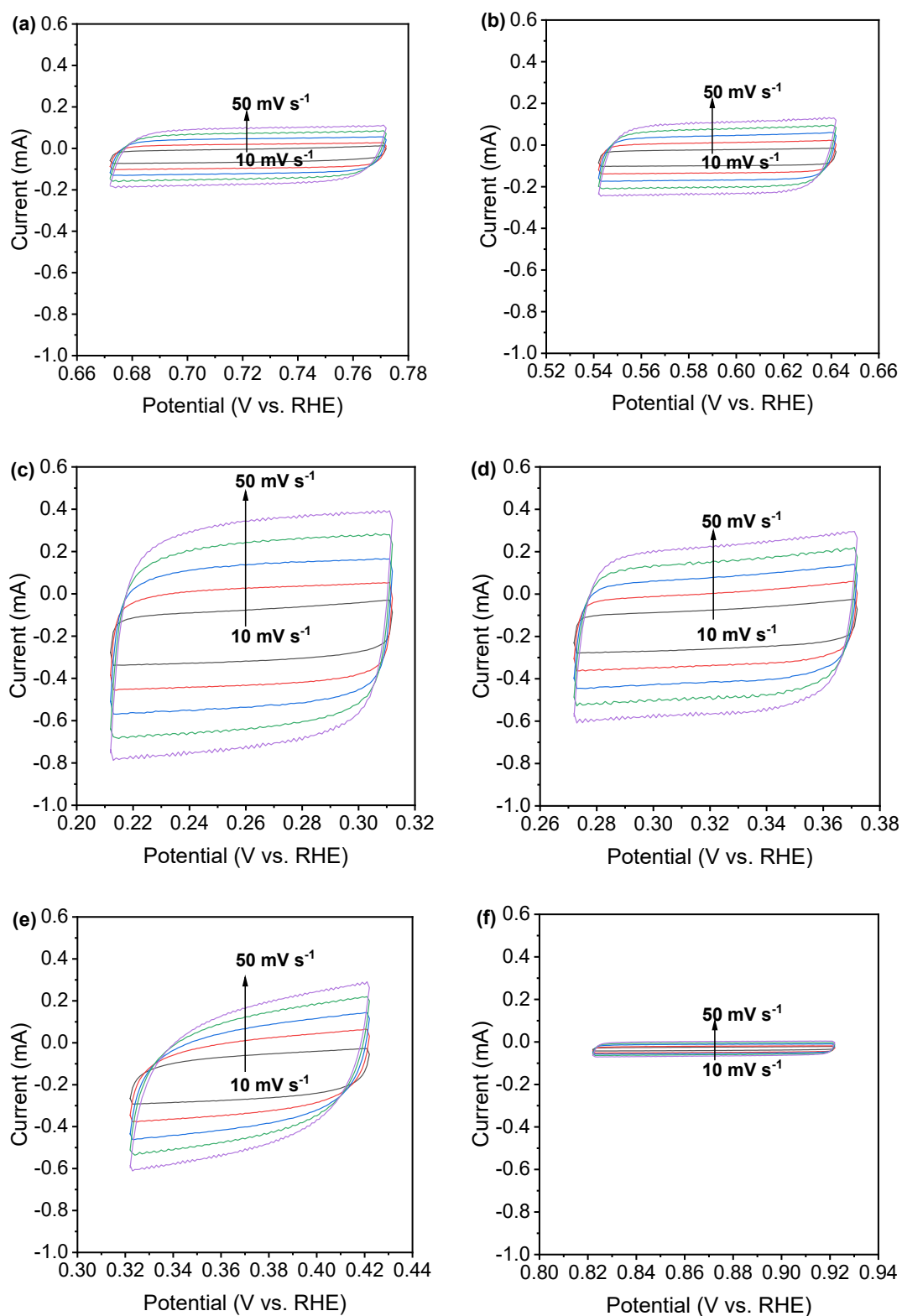
Fig. S23 CV curves at different scan rates for (a) ZIF-67-650N$_2$. (b) ZIF(ZnCo-1:9)-650N$_2$. (c) ZIF(ZnCo-3:7)-650N$_2$. (d) ZIF(ZnCo-5:5)-650N$_2$. (e) ZIF(ZnCo-7:3)-650N$_2$

and (f) ZIF-8-650N$_2$.
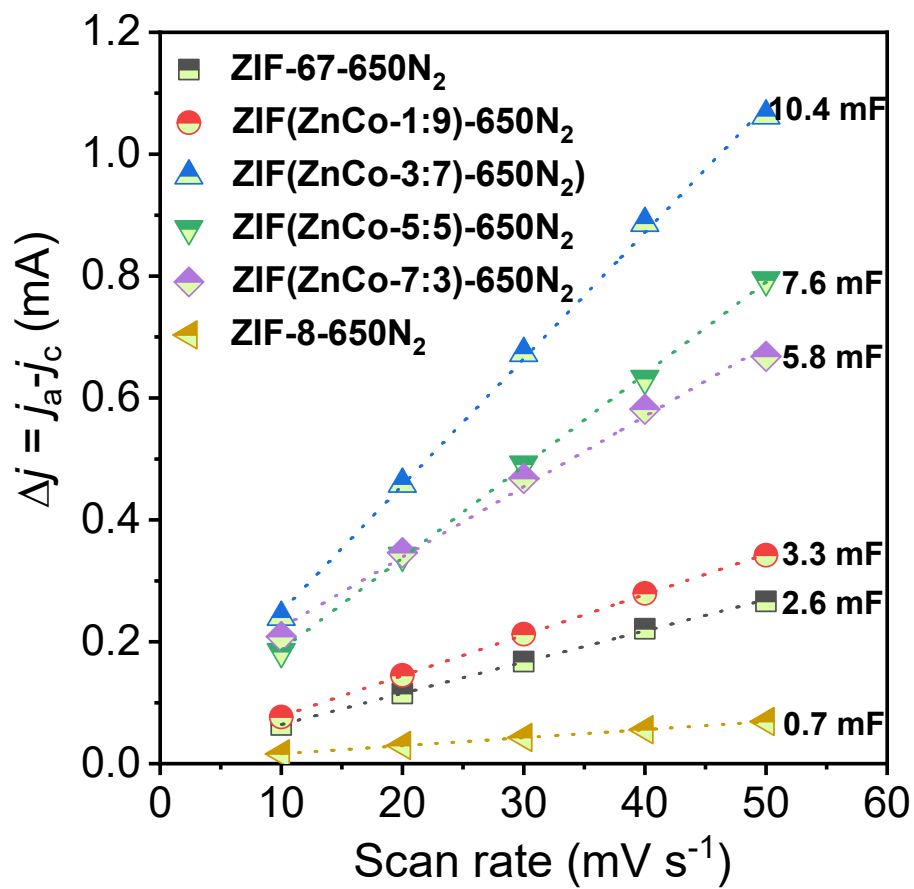
Fig. S24 The plots of the relationships between scan rates and the variations of anode and cathode currents (i.e., $\Delta j = j_a - j_c$).
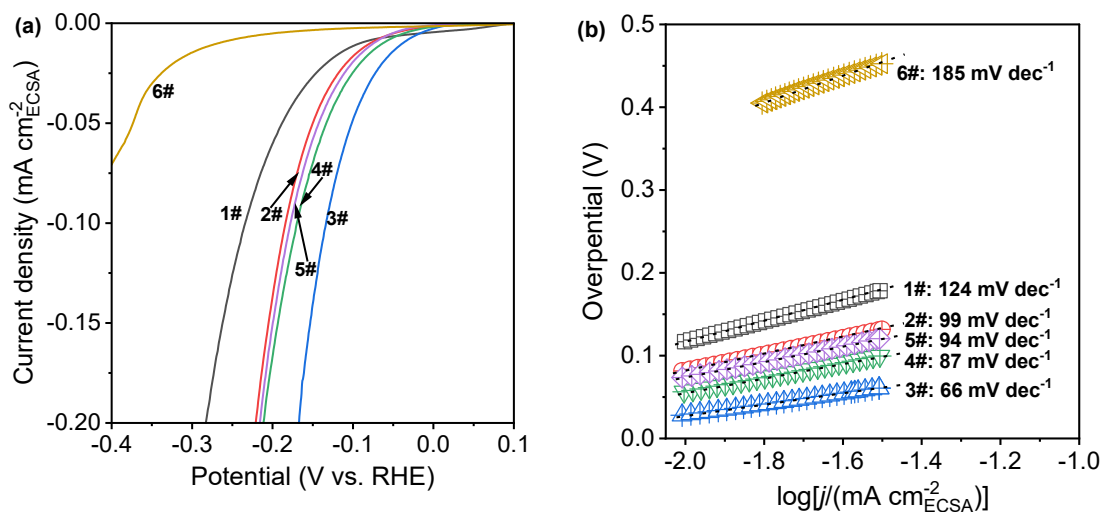
Fig. S25 (a) LSV curves normalized by ECSA. (b) Corresponding Tafel plots. Sample 1#-7# are ZIF-67-650N$_2$, ZIF(ZnCo-1:9)-650N$_2$, ZIF(ZnCo-3:7)-650N$_2$, ZIF(ZnCo-5:5)-650N$_2$, ZIF(ZnCo-7:3)-650N$_2$ and ZIF-8-650N$_2$, respectively.

Note S9 Electrochemical active surface area (ECSA) of the catalysts is used to normalize their LSV curves. The ECSA is calculated by the following equation:

$$ECSA = \frac{C_{dl}}{C_s}$$

(S3)

where C_s is the general specific capacitance for an atomically smooth planar surface under homogeneous electrolyte conditions, C_{dl} is electric double layer capacitance. The C_s is ~0.04 mF cm^{-2} based on a report by Jaramillo et al. [*J. Am. Chem. Soc.*, 2013, **135**, 16977.]. The C_{dl} values of ZIF-67-650N$_2$, ZIF(ZnCo-1:9)-650N$_2$, ZIF(ZnCo-3:7)-650N$_2$, ZIF(ZnCo-5:5)-650N$_2$, and ZIF(ZnCo-7:3)-650N$_2$ and ZIF-8-650N$_2$ are ~2.6, ~3.3, ~10.4, ~7.6, ~5.8, ~0.7 mF, respectively, and the corresponding ECSA values are ~65, ~82.5, ~260, ~190, ~145, ~17.5 cm^2, respectively. After normalization, the obtained LSV curves and Tafel plots are shown in Figs. S25a and S25b, respectively. The Tafel

slopes of ZIF-67-650N$_2$, ZIF(ZnCo-1:9)-650N$_2$, ZIF(ZnCo-3:7)-650N$_2$, ZIF(ZnCo-5:5)-650N$_2$, and ZIF(ZnCo-7:3)-650N$_2$ and ZIF-8-650N$_2$ are ~124, ~99, ~66, ~87, ~94 and ~185 mV dec^{-1}, respectively, which are very close to their pristine Tafel slopes (Table 1 and Fig. 3b). Furthermore, the intrinsic j_{0-ECSA} values, which are also determined by those Tafel plots (Fig. S25b), are ~1.24, ~1.48, ~3.73, ~2.28, ~1.64 and ~0.36 μA cm$^{-2}_{ECSA}$ for ZIF-67-650N$_2$, ZIF(ZnCo-1:9)-650N$_2$, ZIF(ZnCo-3:7)-650N$_2$, ZIF(ZnCo-5:5)-650N$_2$, and ZIF(ZnCo-7:3)-650N$_2$ and ZIF-8-650N$_2$, respectively. Thus, the trend of the intrinsic j_{0-ECSA} well agrees with that of the j_0.
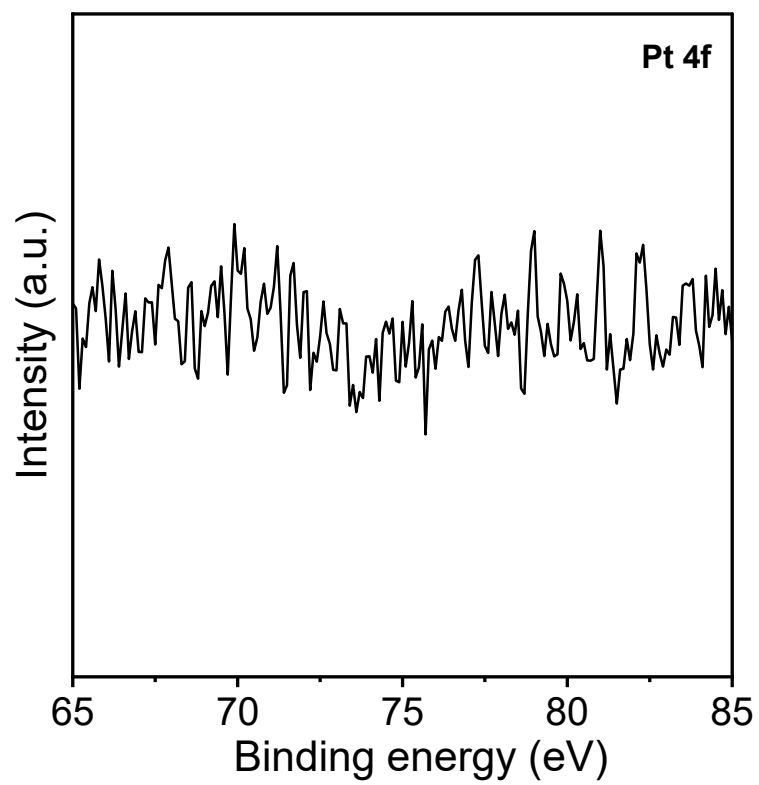
Fig. S26 XPS spectrum of Pt 4f for ZIF(ZnCo-3:7)-650N$_2$

3. Supporting Tables

Table S1 EDS atomic compositions of the resultant catalysts derived from ZIF(ZnCo).

Samples	Co (at%)	Zn (at%)	C (at%)	N (at%)	O (at%)
ZIF(ZnCo-1:9)-650N$_2$	8.37	0.58	81.89	6.92	2.24
ZIF(ZnCo-3:7)-650N$_2$	6.44	1.98	86.28	2.63	2.67
ZIF(ZnCo-5:5)-650N$_2$	5.22	3.30	76.59	9.61	5.28
ZIF(ZnCo-7:3)-650N$_2$	2.83	4.97	68.16	17.06	6.98

Table S2 Surface atomic compositions of the resultant catalysts determined by XPS.

Samples	Co (at%)	Zn (at%)	Zn:Co	C (at%)	N (at%)	O (at%)
ZIF-67-650N$_2$	4.17	0	0	72.16	12.38	11.29
ZIF(ZnCo-1:9)-650N$_2$	3.34	1.57	0.47	76.15	12.47	6.47
ZIF(ZnCo-3:7)-650N$_2$	1.70	2.30	1.35	80.86	8.31	6.83
ZIF(ZnCo-5:5)-650N$_2$	1.38	3.89	2.82	72.91	12.50	9.32
ZIF(ZnCo-7:3)-650N$_2$	1.15	5.00	4.35	69.82	13.03	11.00
ZIF-8-650N$_2$	0	9.05	--	58.82	21.25	10.88

Table S3 Binding energy (eV) of the surface species of the resultant catalysts determined by XPS.

Catalysts	Co 2p$_{3/2}$				Zn 2p$_{3/2}$	N 1s		O 1s		
	Co^0	Co^{3+}	Co^{2+}	Sat.	Zn^{2+}	py-N	pr-N	C-OH	O-C=O	C=O
ZIF-67-650N$_2$	778.42	780.46	782.29	785.96	//	398.81	400.53	530.28	531.21	532.41
ZIF(ZnCo-1:9)-650N$_2$	778.35	779.99	781.95	785.70	1021.82	398.73	400.48	530.71	531.31	532.83
ZIF(ZnCo-3:7)-650N$_2$	778.20	779.63	781.59	784.92	1021.77	398.67	400.43	530.42	531.76	532.90
ZIF(ZnCo-5:5)-650N$_2$	778.15	779.59	781.57	784.55	1021.71	398.63	400.40	531.03	531.77	533.01
ZIF(ZnCo-7:3)-650N$_2$	778.13	779.57	781.55	784.30	1021.68	398.60	400.23	531.12	531.92	533.10
ZIF-8-650N$_2$	//	//	//	//	1021.52	398.50	400.10	531.31	532.13	533.38

Table S4 Summary of HER activity of the resultant catalysts and 20 wt.% Pt/C in 1 M KOH.

Samples	η_{10} (mV)	η_{1000} (mV)	Tafel slope (mV dec^{-1})	j_0 (mA cm^{-2})	$j_{0\text{-ECSA}}$ (mA cm^{-2})
ZIF-67-650N$_2$	131	--	134	1.05	1.24
ZIF(ZnCo-1:9)-650N$_2$	91	358	102	1.25	1.48
ZIF(ZnCo-3:7)-650N$_2$	16	219	65	5.70	3.73
ZIF(ZnCo-5:5)-650N$_2$	47	305	87	2.91	2.28
ZIF(ZnCo-7:3)-650N$_2$	73	315	98	1.81	1.64
ZIF-8-650N$_2$	400	--	187	0.07	0.36
20 wt.% Pt/C	25	--	39	2.42	--

Table S5 Summary of the recently-developed catalysts for HER with high currents.

Catalysts	Electrode	Electrolyte	Mass loading (mg cm^{-2})	η at low current density (mV)	η_{1000} (mV)	Tafel slope (mV dec^{-1})	Reference
ZIF(ZnCo-3:7)-650N$_2$	*GC*	*1 M KOH*	*0.5*	*16@10 mA cm^{-2}* *179@500 mA cm^{-2}*	*219*	*65*	*This work*
Ni$_2$P nanoarray	Ni foam	1 M KOH	3.83	--	306	76	S1
Amorphous-NiCo LDH	Ni foam	1 M KOH	3.15	36@10 mA cm^{-2}	286	57	S2
W, Mo co-doped NiCoP	Ni foam	1 M KOH	--	55@10 mA cm^{-2}	249	42.3	S3
Fe-Ni$_2$P@C/NF	Ni foam	1 M KOH	--	294@500 mA cm^{-2}	313	45	S4
NiCo@C-NiCoMoO	Ni foam	1 M KOH	10.5	39@10 mA cm^{-2}	266	63.5	S5
Ni-FeO$_x$/FeNi$_3$/NF	Ni foam	1 M KOH	4	35@10 mA cm^{-2}	272	44.6	S6
NiP$_2$@MoO$_2$/Co(Ni)MoO$_4$	Ni foam	1 M KOH	100	66@50 mA cm^{-2}	297	165.2	S7
NiCoP	Ni foam	1 M KOH	2.61	171@500 mA cm^{-2}	193	54	S8

Ni-MoN/NF	Ni foam	1 M KOH	--	37.36@10 mA cm^{-2}	283.83	57.6	S9
CoFeOH/CoFeP	Fe foam	1 M KOH	--	194.9@500 mA cm^{-2}	221.8	128.37	S10
F, P-Fe$_3$O$_4$	Fe foam	1 M KOH	--	179.5@100 mA cm^{-2}	321.3	127.9	S11
F-Co$_2$P/Fe$_2$P	Fe foam	1 M KOH	--	229.8@500 mA cm^{-2}	260.5	115.01	S12
Porous Co-P	Co foam	1 M KOH		243@500 mA cm^{-2}	290	78	S13
Fe$_2$P-Co$_2$P	Co foam	1 M KOH	~6	81@10 mA cm^{-2}	254	56	S14
HC-MoS$_2$/Mo$_2$C	Cu foam	0.5 M H$_2$SO$_4$	10	~400@250 mA cm^{-2}	412	60	S15
Pt nanoparticles	Cu foam	1 M phosphate-buffered solution (PBS)	0.3	35@10 mA cm^{-2}	438	61	S16
Single-atom Co-N-C	Aligned porous carbon film	0.5 M H$_2$SO$_4$	0.5 wt% of Co	272@500 mA cm^{-2}	343	67.6	S17
Co, Se co-doped MoS$_2$	Carbon	0.5 M H$_2$SO$_4$	4	104@10 mA cm^{-2} on	382	67	S18

nanofoam	fiber paper			GC with a loading of 0.5 mg cm^{-2}			
NiMnFeMo alloy	Free-standing nanoporous NiMnFeMo alloy	1 M KOH	--	178@500 mA cm^{-2}	290	32	S19
MoS$_x$-Fe@UiO-66-(OH)$_2$	GC	0.5 M H$_2$SO$_4$	0.283	118@10 mA cm^{-2}	297	41	S20

Table S6 Surface compositions of ZIF(ZnCo-3:7)-650N$_2$ before and after CV cycling.

CV cycling	Co (at%)				N (at%)			O (at%)			
	Co^0	Co^{3+}	Co^{2+}	Total Co	py-N	pr-N	Total N	C=O	O-C=O	C-OH	Total O
Before	0.61	0.57	0.52	**1.70**	5.71	2.60	**8.31**	1.17	3.37	2.29	**6.83**
After	0.44	0.63	0.61	**1.68**	4.83	3.12	**7.95**	1.77	3.48	4.02	**9.27**

Supporting references

S1 X. Yu, Z.-Y. Yu, X.-L. Zhang, Y.-R. Zheng, Y. Duan, Q. Gao, R. Wu, B. Sun, M.-R. Gao, G. Wang, S.-H. Yu, *J. Am. Chem. Soc.*, 2019, **141**, 7537.

S2 H. Yang, Z. Chen, P. Guo, B. Fei, R. Wu, *Appl. Catal., B*, 2020, **261**, 118240.

S3 X. Guo, M. Li, L. He, S. Geng, F. Tian, Y. Song, W. Yang, Y. Yu, *Nanoscale*, 2021, **13**, 14179.

S4 D. Li, Z. Y. Li, R. Zou, G. Shi, Y. M. Huang, W. Yang, W. Yang, C. F. Liu, X. W. Peng, *Appl. Catal., B*, 2022, **307**, 121170.

S5 G. Qian, J. Chen, T. Yu, L. Luo, S. Yin, *Nano-Micro Lett.*, 2021, **13**, 77.

S6 A. Qayum, X. Peng, J. F. Yuan, Y. D. Qu, J. H. Zhou, Z. L. Huang, H. Xia, Z. Liu, D. Q. Tan, P. K. Chu, F. S. Lu, L. S. Hu, *ACS Appl. Mater. Interfaces* 2022, **14,** 27842-27853.

S7 Q. Xu, P. C. Wang, L. Wan, Z Xu, M. Z. S, B. G. Wang, *ACS Appl. Mater. Interfaces* 2022, *14*, 19448-19458.

S8 L. F. Li, W. R. Zou, Q. L. Ye, Q. L, Q. S. Feng, J. R. Wei, X. T. Xu, F. Wang, *J. Power Sources*. 2021, **516,** 230657.

S9 J. H. Sun, F. F. Guo, X. Y. Li, J. Yang, J. F. Ma, *Sustainable Energy Fuels*, 2021, **5,** 5565-5573.

S10 X.-Y. Zhang, F.-L. Wang, J.-Y. Fu, Y.-N. Zhen, B. Dong, Y.-N. Zhou, H.-J. Liu, D.-P. Liu, C.-G. Liu, Y.-M. Chai, *J. Power Sources*, 2021, **507**, 230279.

S11 X.-Y. Zhang, F.-T. Li, R.-Y. Fan, J. Zhao, B. Dong, F.-L. Wang, H.-J. Liu, J.-F. Yu, C.-G. Liu, Y.-M. Chai, *J. Mater. Chem. A*, 2021, **9**, 15836.

S12 X.-Y. Zhang, Y.-R. Zhu, Y. Chen, S.-Y. Dou, X.-Y. Chen, B. Dong, B.-Y. Guo, D.-P. Liu, C.-G. Liu, Y.-M. Chai, *Chem. Eng. J.*, 2020, **399**, 125831.

S13 Y. Li, B. Wei, Z. Yu, O. Bondarchuk, A. Araujo, I. Amorim, N. Zhang, J. Xu, I. C. Neves, L. Liu, *ACS Sustainable Chem. Eng.* 2020, *8*, 10193.

S14 X. Liu, Y. Yao, H. Zhang, L. Pan, C. Shi, X. Zhang, Z.-F. Huang, J.-J. Zou, *ACS Sustainable Chem. Eng.* 2020, *8*, 17828.

S15 C. Zhang, Y. Luo, J. Tan, Q. Yu, F. Yang, Z. Zhang, L. Yang, H.-M. Cheng, B. Liu, *Nat. Commun.* 2020, **11**, 3724.

S16 Y. Tan, R. Xie, S. Zhao, X. Lu, L. Liu, F. Zhao, C. Li, H. Jiang, G. Chai, D. J. L. Brett, P. R. Shearing, G. He, I. P. Parkin, *Adv. Funct. Mater.*, 2021, **31**, 2105579.

S17 R. Liu, Z. Gong, J. Liu, J. Dong, J. Liao, H. Liu, H. Huang, J. Liu, M. Yan, K. Huang, H. Gong, J. Zhu, C. Cui, G. Ye, H. Fei, *Adv. Mater.*, 2021, **33**, 2103533.

S18 Z. Zheng, L. Yu, M. Gao, X. Chen, W. Zhou, C. Ma, L. Wu, J. Zhu, X. Meng, J. Hu, Y. Tu, S. Wu, J. Mao, Z. Tian, D. Deng, *Nat. Commun.* 2020, *11*, 3315.

S19 H. Liu, C. Xi, J. Xin, G. Zhang, S. Zhang, Z. Zhang, Q. Huang, J. Li, H. Liu, J. Kang, *Chem. Eng. J.*, 2021, 404, 126530.

S20 L. Zhang, Z. Yan, X. Chen, M. Yu, F. Liu, F. Cheng, J. Chen, *Chem. Commun.*, 2020, 56, 2763.